Charles University in Prague

Faculty of Mathematics and Physics

MASTER THESIS

Jakub Kandra

Simulation of Belle II physics events and performance tests of reconstruction software

Institute of Nuclear and Particle Physics

Supervisor of the master thesis: RNDr. Peter Kvasnička
Study programme: Physics
Study branch: Nuclear and Particle Physics

Prague 2016

I declare that I carried out this master thesis independently, and only with the cited sources, literature and other professional sources.

I understand that my work relates to the rights and obligations under the Act No. 121/2000 Sb., the Copyright Act, as amended, in particular the fact that the Charles University in Prague has the right to conclude a license agreement on the use of this work as a school work pursuant to Section 60 subsection 1 of the Copyright Act.

In .... date .... signature of the author

Názov: Simulace fyzikalních procesů v experimentu Belle II a testování kvality rekonstrukčního softwaru

Autor: Jakub Kandra

Katedra: Ústav časticové a jaderné fyziky

Vedoucí diplomové práce: RNDr. Peter Kvasnička, Ústav částicové a jaderné fyziky

Abstrakt: Táto práca je venovaná štúdiu alignmentu vrcholových polovodičových detektorov experimentu Belle II. Je rozdelená do niekoľkých častí. Prvá časť predstavuje experiment Belle II ako B-továreň novej generácie, s jej ambicióznymi plánmi naberania dát a fyzikálnej analýzy. Na to nadväzuje popis vrcholových detektorov a softwarových nástrojov určených na kalibráciu a alignment detektorov. Ťažiskovou časťou je štúdia fyzikálnych procesov, využívaných pre kalibráciu detektora, spojená s hľadaním najvhodnejšieho riešenia pre priebežnú aplikáciu počas zberu nameraných dát. Následne boli testované softwarové nástroje na rozladenej geometrii, aby sme zistili ich odolnosť voči rozladeniu geometrie. Bola prevedená aj štúdia vplyvu rozladenia geometrie (misalignmentu) na pozorovateľné parametre pri analýze vybraných fyzikálnych procesov. V poslednej časti popisujeme vývoj monitorovacieho nástroja pre priebežnú diagnostiku rozladenia geometrie alebo konfigurácie detektora. Takýto nástroj bude sledovať nepresnosti v rekonštrukcii fyzikálnych pozorovateľných a signalizovať, ak táto nepresnoť prekročí nastavené medze.

Klíčová slova: Belle II, generátor srážek, křemíkový detektor, rekonstrukce drah částic, alignment

Title: Simulation of Belle II physics events and performance tests of reconstruction software

Author: Jakub Kandra

Institute: Institute of Nuclear and Particle Physics

Supervisor: RNDr. Peter Kvasnička, Institute of Nuclear and Particle Physics

Abstract: This thesis is about the alignment of vertex semiconductor detectors of the Belle II experiment. It is divided into several sections. The first part introduces the Belle II experiment as a new generation B-factory, with its ambitious plans of data taking and physical analysis. The second part follows with a more detailed description of Belle II detector and software tools designed for their alignment and calibration. The central part of the thesis describes physical processes used for calibration of the vertex detector, connected with the search of an optimal solution for run-time monitoring and calibration of the detector. We also tested the effect of misalignment on the Belle II tracking software. The following part gives results of the study of misalignment effects on physical observables related to analysis of selected physical channels. The last part describes the development of a data quality monitoring tool for the tracking system. The tools has to provide a run-time diagnostic of misalignment and miscalibration by monitoring the precision and accuracy of reconstruction of physical observables.

Keywords: Belle II, physics generator, silicon detector, tracking, alignment

I would like to thank my supervisor Peter Kvasnicka for opportunity to cooperate at Belle II experiment and for his patience during discussions about alignment and tracking system of Belle II and other topics. I would also like to thank all staff of Belle II Prague group for participation at Belle II general meeting and tracking meeting. The discussions at the meeting helped me to understand alignment issues and I had a possibility to present my results to an audience of experts. I would like to thank Tadeas Bilka for sharing his knowledge about alignment procedure and scripts for using alignment tools.

The section about validation of alignment tracking system is based on my Summer student program 2015 at DESY in Hamburg. I would like to thank my supervisor Sergey Yashchenko and all staff of the Belle II group at DESY. During that summer I gained a lot of knowledge about alignment validation, generators, track finders and the CDC.

Contents

Introduction

In particle physics, flavour is the property that distinguishes different families of basic building blocks of matter. The flavour defines six members of the lepton sector (the electron, the muon, the tau, the electron-neutrino, the muon-neutrino and the tau-neutrino) and six quarks (designated up, down, charm, strange, top and bottom). Flavour physics studies interactions that distinguish between flavours. The gauge interactions that are related to unbroken symmetries and mediated therefore by massless gauge bosons do not distinguish among flavours and do not constitute part of flavour physics [1].

CP Violation

CP violation is the violation of the combined conservation laws associated with charge conjugation (C) and parity (P). Charge conjugation is a mathematical operation that reverses sign of additive quantum numbers, thus changing particles to antiparticles and vice versa. Charge conjugation implies that every charged particle has an opposite-charged antimatter counterpart, or antiparticle. Parity, or space inversion, is the reflection in the origin of the space coordinates of a particle or a particle system.

For years it was assumed that charge conjugation and parity were exact symmetries of elementary processes. Since 1964 experiments have demonstrated that CP symmetry is violated. The first demonstration of CP violation was done using the electrically neutral K meson [2].

In 1972 M. Kobayashi and T. Maskawa published their explanation of CP violation [3]. The theory predicted CKM (Cabibbo–Kobayashi–Maskawa) mixing matrix and three generations of fundamental particles. The CKM matrix is a unitary matrix and can be parametrized by three real mixing angles and one complex phase. The CKM parameters can be shown as unitary triangle in phase space, which is parametrized via $\bar{\eta}$ and $\bar{\rho}$ (Fig. 1) [4]. Since publishing of the Kobayashi-Maskawa theory physicists wanted to test the theory and discover the third generation of quarks. The quarks have been discovered in the 1980's and 1990's [5] [6] [7]. Kobayashi and Maskawa were for their theory awarded by Nobel prize in 2008 [8]. The universality of the KM idea can be shown via the mixing matrix in lepton sector. The mixing matrix in lepton sector is used for explanation of neutrino oscillations. This theory predicts that neutrino has mass. In this case T. Kajita and A. B. McDonald were awarded Nobel Prize in 2015 for the discovery of neutrino oscillations [9].

CP violation in experiments

CP violation can be measured by $\mathrm{K}_{S,L} \to \pi\pi$ decay rates (e.g. NA48 experiment [10] and other) or measurement of CKM parameters by very rare decays, such as $\mathrm{K} \to \pi l^+ l^-$ by NA62 experiment [11].

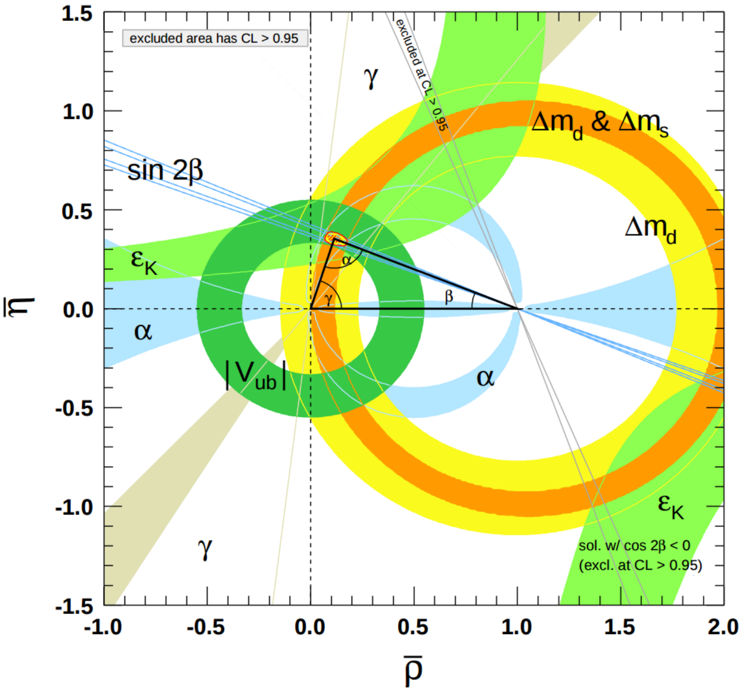

Figure 1: *The Unitary triangle:* The CKM parameters are α, β and γ angles of the triangle in the $\bar{\rho}$, $\bar{\eta}$ phase space. The coloured objects describe constraints for CKM parameters.

Many experiments used B - decays for measurement of CP violation. These experiments are called "B factories" [12]. The famous B factories were the Belle and BaBar experiments that laid ground for the Nobel Prize in 2008. The "golden observable" for B factories is the CP asymmetry between $\mathrm{B}^0 \rightarrow \mathrm{J}/\psi\mathrm{K}^0_S$ and $\bar{\mathrm{B}}^0 \rightarrow J/\psi \mathrm{K}^0_S$. The B factories produce neutral mesons in pairs at centre-of-mass energy corresponding to the $\Upsilon(4S)$ resonance. The technique for performing the interference measurement is illustrated in Fig 2. The produced pair is entangled in coherent quantum state until one of the mesons decays. Some of B^0 meson decays produce a flavour-specific final state, i. e., the final-state particles can be used to determine whether the decaying meson was a B^0 or a $\bar{\mathrm{B}}^0$. Such a decay is called a "flavour-tag" decay. At the time this B meson decays, the accompanying B meson's flavour is constrained to being the opposite.

Every B factory must satisfy the baseline requirements for an experiment to measure the CP violating phases using the time-dependent CP asymmetry technique. The requirements are boosted $\mathrm{B}^0\bar{\mathrm{B}}^0$ pairs, high luminosity, and high spatial resolution and large-coverage detector with excellent particle identification. The B^0 and $\bar{\mathrm{B}}^0$ mesons must have decay lengths in laboratory long enough for the time sequence of their decays to be measured. This is achieved by an asymmetric energy of collisions in the laboratory frame. Because of a better resolution at the energy of the $\Upsilon(4S)$ resonance, bunches of electrons and positrons are used for collisions. For an e^+e^- collider operating at $\Upsilon(4S)$, this requires integrated luminosities of at least $\sim$ 30 fb^{-1}, because of branching ratio of $B^0 \rightarrow J/\psi K^0_{short}$ [12]. Historically the newest approach is using B mesons produced in hadron collisions by the LHCb experiment.

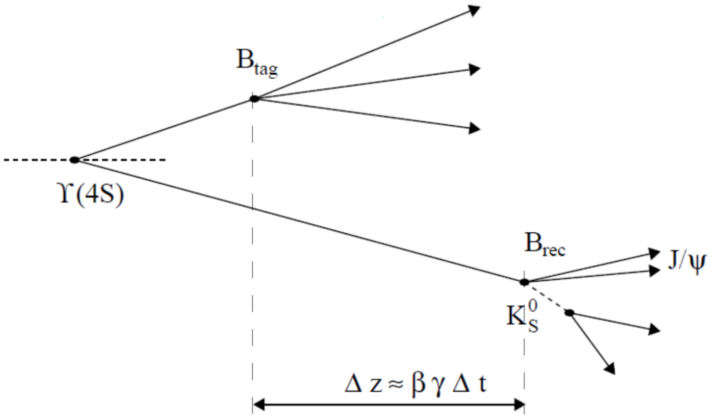

Figure 2: *Measurement of CP violation using B decays:* The $\Upsilon(4S)$ particle decays into a pair of neutral B mesons. CP violation is determined from the distributions of differences between the vertices of both reconstructed neutral B mesons. The difference can be expressed in terms of time or position difference.

Belle II is an experiment under construction at the High Energy Accelerator Research Organization (高エネルギー加速器研究機構) in Tsukuba, Ibaraki prefecture, Japan. The Belle II experiment is an upgrade of the Belle experiment and expected integrated luminosity is 50 times higher than in the previous experiment. Belle II will continue and extend the physics program of Belle which finished operations in 2010. The main goal of Belle II is to continue the study of CP violation in B-meson decays. The Belle II program is extended in several directions, e.g., to the search of new physics in rare processes.

Alignment and calibration

In order to precisely reconstruct the decay vertex position of both B mesons in an event and the proper time difference between their decays, accurate information is required on the position of the reconstructed detector hits left by charged particles travelling through the tracking volume. To determine the position of hits in 3D space, an extremely precise information in needed on the position of the detector in space. This information cannot be usually obtained to satisfactory precision during detector installation, and is acquired and updated during experiment operation by analysis of particle tracks. This procedure is called detector alignment.

The present study deals with optimization of alignment procedure using the data of different physical processes. After alignment and calibration parameters of the detectors are determined, it is necessary to check if the achieved accuracy is sufficient for the physics analysis.

During data collection, is it necessary to keep track of the status of geometry alignment and calibration. As ambient conditions may change during prolonged runs, the geometry components may move or deform, and detector parameters may vary with time as well. Sensitive detection of departures of geometry or configuration from an initial state is often based on monitoring of known physical parameters, such as well-known processes or parameters constrained by symmetries. Monte Carlo studies are used to make a link between such parameters and misalignment or miscalibration. By monitoring the accuracy or precision of reconstruction of the critical physical parameters, a flag can be raised when the quality of reconstruction decreases due to misalignment or miscalibration.

The motivation of this thesis is an alignment and calibration study of the Belle II tracking system. This thesis also describes the development of validation procedure used in the Belle II analysis framework.

The review part consists of two chapters. The first describes the SuperKEKB accelerator and the Belle II detector. The second explains alignment procedures.

The results part contains four chapters. The first contains results of alignment of the Belle II silicon vertex detector. The second describes convergence of alignment. The third shows the effects of misalignment on physical analysis. The fourth explains alignment validation and monitoring.

1. The Belle II detector

The Belle detector ran on the KEKB e^+e^- asymmetric energy collider between 1999 and 2010 [13]. The experiment was designed and optimized for observation of CP violation in the B meson system (Fig 1.2). In 2001, Belle was indeed able to observe CP asymmetries in B decay, which were expected and consistent with the KM theory. The Belle spectrometer was a general purpose device with reasonable solid coverage as well as high quality vertexing with silicon strip detectors, charged particle tracking with central drift chamber, and excellent electromagnetic calorimetry as well as muon and K_L detection. These detector capabilities allowed Belle to not only cover most of the important topics in B physics, but also to make important discoveries in charm physics, tau lepton physics, hadron spectrometry and two-photon physics. KEKB was designed to run on or near the $\Upsilon(4S)$ resonance, which is the optimal center of mass energy for the production of B$\bar{\text{B}}$ pairs. However, Belle also recorded a series of unique data sets at the $\Upsilon(1S)$, $\Upsilon(2S)$ and $\Upsilon(5S)$ resonances. KEKB broke all records for integrated and instantaneous luminosity for a high energy accelerator (Fig 1.1). As a result, Belle was able to integrate over one inverse attobarn of data.

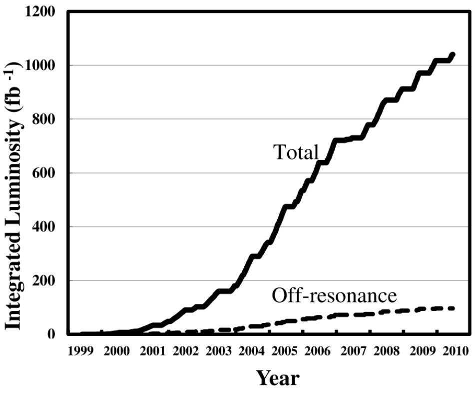

Figure 1.1: The historical record of Belle integrated luminosity

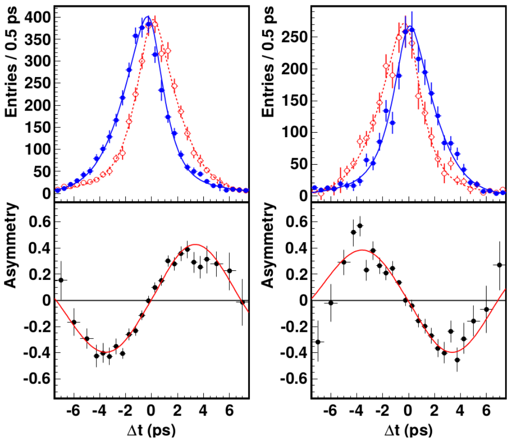

Figure 1.2: *The CP violation by the Belle experiment:* The left column of figures shows $c\bar{c}K_S^0$ events and right column shows J/ΨK$_L^0$ events. The red lines correspond to particles composed of positively charged quarks and blue lines correspond to particles of negatively charged quarks.

1.1 The Belle II detector at SuperKEKB

SuperKEKB, which is the upgrade of the KEKB B factory, is a next generation high luminosity electron-positron collider with asymmetric energies. The upgraded accelerator is designed to produce $\sim$ 50 ab^{-1} collisions [14]. The collider can provide a clean environment for production of B meson pairs via $\Upsilon(4S)$ resonance decay. The integrated luminosity corresponds to 55 billion of B$\bar{\text{B}}$ pairs, 47 billion of $\tau^+\tau^-$ pairs and 65 billion of $c\bar{c}$ states.

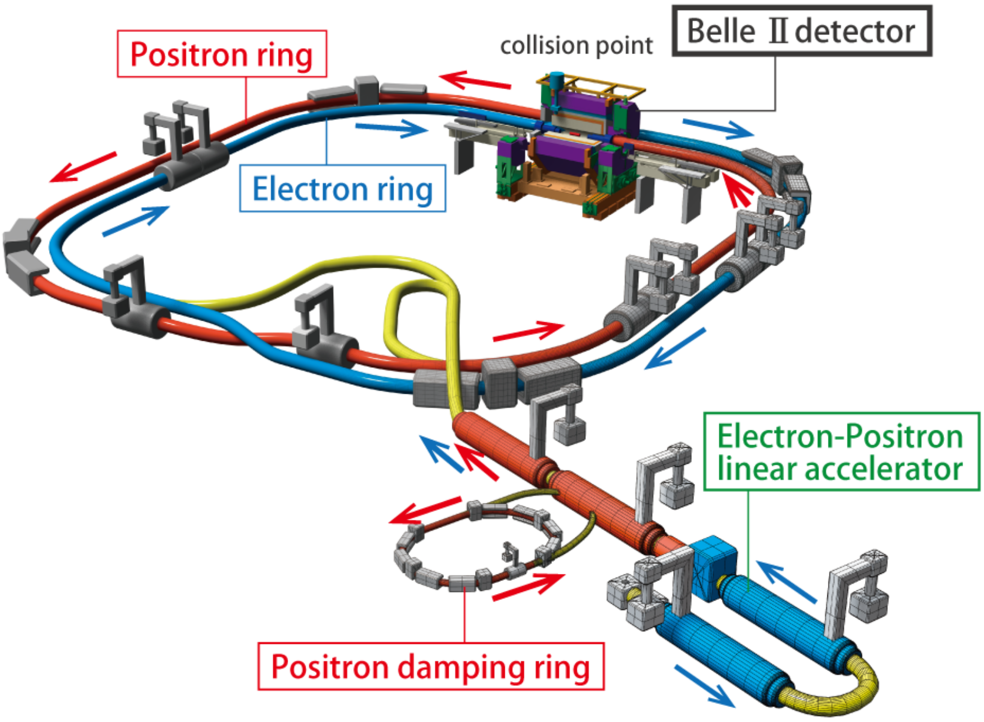

Figure 1.3: *Schematic view of SuperKEKB:* The drawing shows all relevant collider system components that produce and deliver electrons and positrons to interaction point.

SuperKEKB is a double-ring collider (Fig. 1.3), the beam energy of the positrons (LER for low energy ring) is 4 GeV and that of the electrons (HER for high energy ring) is 7 GeV. Since continuous injection is necessary to maintain constant luminosity with a short beam lifetime, simultaneous injection among rings is required at SuperKEKB. Further requirements are a shorter beam intensity per pulse and low emittance for both electrons and positrons because the lifetime of the main rings will be very short at design beam currents and the injection aperture will be small. A photo-cathode RF gun is adopted to produce electrons and a flux concentrator is used to produce positron beams. Two-bunch-per-pulse injection is considered as well as increasing the beam intensity per pulse. Since the positrons coming from the flux concentrator have a large emittance, a damping ring is necessary to make the positron emittance small. The positron beam is accelerated up to 1.1 GeV by a linear accelerator and extracted to inject into the damping ring. The positron beam is injected to the linear accelerator again, then accelerated up to 4 GeV and injected to LER. After production electrons are accelerated to 7 GeV by the linear accelerator and injected to HER.

Beam collisions are kept during continuous injection. Nano-beam large-angle crossing angle collision scheme is used. This scheme is based on a large crossing angle, small horizontal and vertical emittances. The crossing angle itself can be larger than in the machines generation before. The situation of the nano-beam crossing is similar to a collision with many micro bunches which have a short bunch length. The bunch crossing at interaction point is reduced to twentieth of bunch crossing of KEKB (Fig. 1.4).

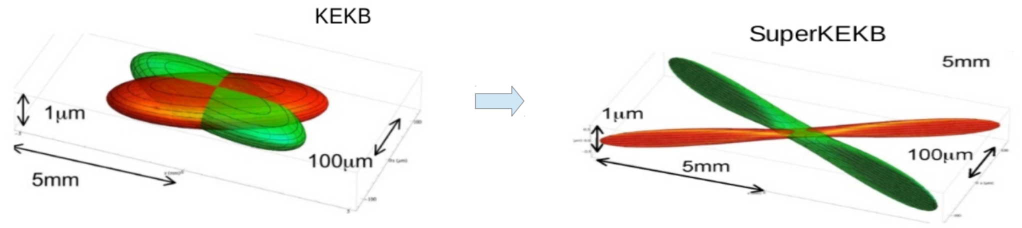

Figure 1.4: Bunch crossing of KEKB (left) and SuperKEKB (right) at the intersection point

The particles produced in a collision fly from the interaction point (IP) into the volume of the Belle II detector (Fig. 1.5). The Belle II detector is mostly composed of upgraded Belle sub-detectors. The vertex detection system (VXD) is composed of a new silicon pixel detector (PXD) and strip detector (SVD). The tracking system includes the central drift chamber (CDC) and VXD. The particle identification (PID) system consists of TOP detector at the barrel and ARICH detector in forward endcap part. Energy of electromagnetic particles is measured by electromagnetic calorimeter (ECL). Long lived kaons and muons are detected by the KLM system.

1.2 The pixel detector

The beam-pipe radius at the interaction point will only be about 10 mm. The large expected background occupancy excludes strip detectors at radii below 40 mm. Therefore, pixel sensors form the two innermost layers. Because of extreme luminosity, necessity of very precise vertex reconstruction and requirement of minimalistic material budget, the thickness of PXD sensors is only 75 μm [16]. The PXD consists of two layers (Table 1.1). A ladder size of first layer is 15 × 136 mm^2 and second layer is 15 × 170 mm^2. Pixel size of sensors in outer region of first layer, marked 1.*.1 in Fig. 1.10, is 50 × 60 μm^2 and in the central region sensors it is (1.*.2) is 50 × 55 μm^2. In the second layer pixel size for the outer region is 50 × 85 μm^2 and for central region it is 50 × 70 μm^2.

The PXD sensors are based on the DEPFET (DEPleted Field Effect Transistor) technology [17]. It is a semiconductor detector concept that combines detection and in-pixel amplification. It was invented by Josef Kemmer and Gerhard Lutz. The large scale fabrication is done by the Max Plank's Institute Semiconductor laboratory. Detectors based on DEPFET technology are now considered for implementation in several projects in the fields of astrophysics (BepiColombo [19],

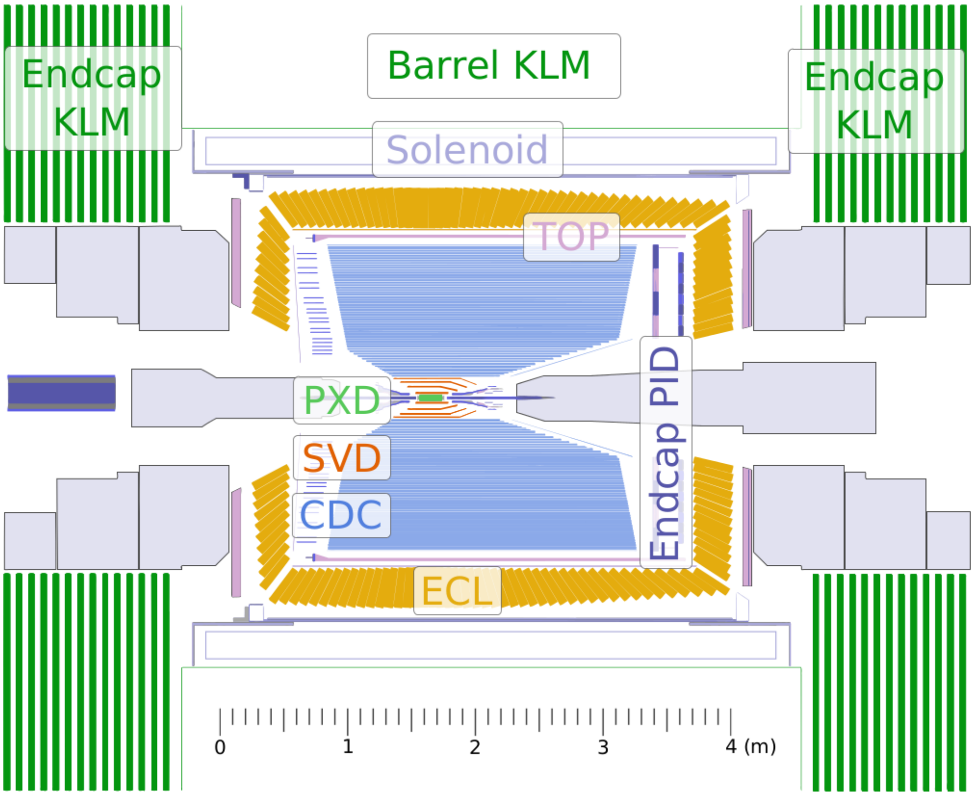

Figure 1.5: *Schematic cross-section of the Belle II detector:* This figure shows all subdetectors. The **PXD** (light green), the **SVD** (orange) and the **CDC** (blue) compose the tracking system. The **TOP** (pink) and **endcap PID** as the **ARICH** (violet) detector are particle identification detectors. The crystals of the **ECL** (yellow) surround the PID detectors. The outermost detectors are the **barrel** and **endcap KLM** (dark green) [15].

ATHENA [18]), photon science (XFEL [20]) and high energy particle physics (ILC [18]).

According to Fig. 1.6 a p- channel is integrated onto a silicon detector substrate, which becomes fully depleted by a sufficiently high negative voltage to a p+ contact on the back side. The doping profile of the bulk forms a minimum of the potential for electrons in a small region under the transistor gate channel. Incident particles generate electron-hole pairs within the fully depleted bulk. While the holes drift to the back contact, electrons are accumulated in the potential minimum. When the transistor is switched on, the electrons modulate the channel current. The signal charge and electrons from thermal noise are removed by increasing voltage on the clear (n+) contact. The readout is non-destructive and can be repeated many times.
Cleargate and Clear contact are connected across rows of DEPFET cells (Fig. 1.7). The source and drain contacts are connected across columns. After a row of the matrix has been selected via the gate contact, all cells in this row can be read.

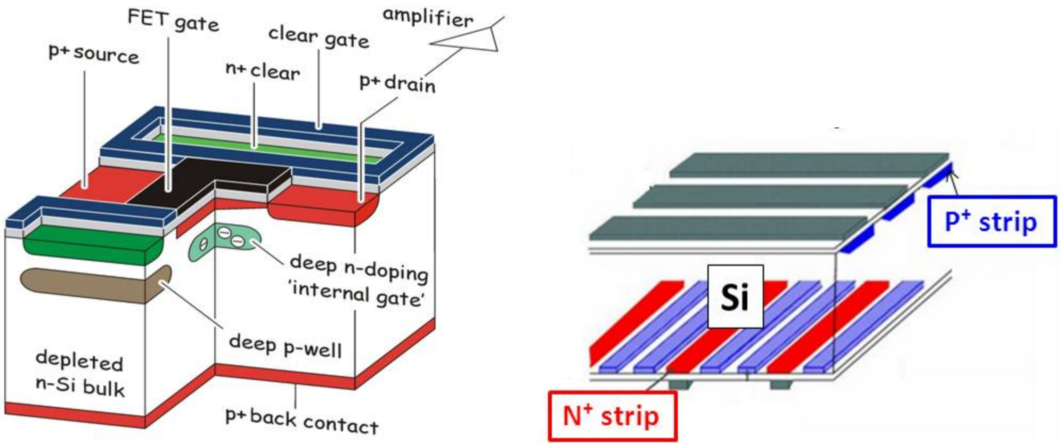

Figure 1.6: *The PXD and SVD sensors:* A DEPFET pixel (left side) and strips in the double-side SVD sensor (right side)

All other cells are turned off at this moment, and no current can flow between source and drain. Depending on the design the activated line can be read using either the source or the drain contact. Thereafter, the signal charges are erased from all the pixels of this line over the Cleargate- and clear contact. A second measurement is done, now with an empty internal gate, serving as a reference measurement. The difference between the two signals corresponds to the actual signal. After selecting the next line, the cycle starts all over again.

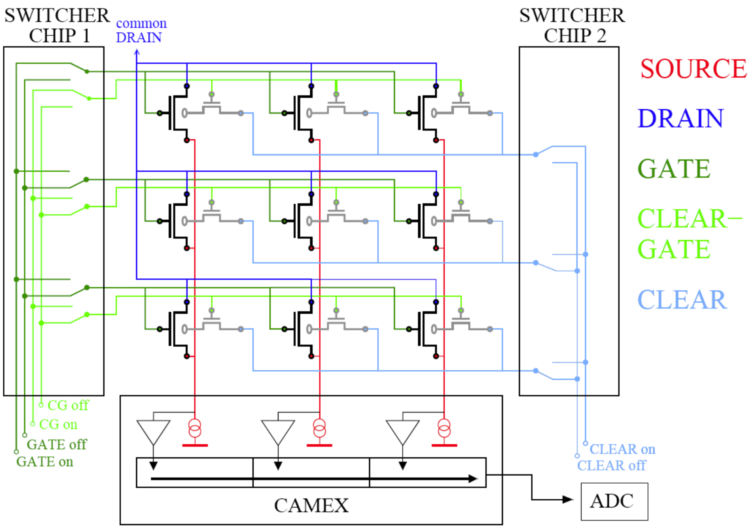

Figure 1.7: *DEPFET pixel matrix with readout system:* The readout system of DEPFET sensors is composed by switcher chips and source.

1.3 The strip vertex detector

The strip vertex detector (SVD) forms the outer part of the vertex detector. The SVD covers the full Belle II angular acceptance of $17° < \theta < 150°$. The SVD is able to reconstruct low-p_t tracks, down to a few tens of MeV/c. This is particularly important for reconstruction of the D* daughters. It is able to reconstruct K$_S$ mesons that decay outside of the PXD volume. The requirements on the SVD are very low dead-time, mechanical stability, low mass and operation reliability.

Double-sided silicon strip detectors (DSSD) are used. The basic geometry of the strip, which includes orthogonally implanted n and p strips on both sides of the detector (Fig. 1.6), provides two coordinate measurements for traversing particles.

When a charged particle passes through the DSSD sensor, the particle deposits its energy in the sensor, and electron-hole pairs are generated along the path. Since the electrons have negative charge, they will be collected by N^+ strips, and holes will be collected by the P^+ strips. They are observed as electric signals, and we can obtain two coordinates of the particle thanks to the mutually perpendicular strips: z direction is read by P-side and $r - \theta$ direction is read by N^- side.

The detector is composed of 4 layers (Table 1.1). The thickness of SVD sensors is 320 μm [21]. Two different sensor shapes are used: rectangular sensors, which will be installed the barrel part, and trapezoidal-shape sensors to cover the forward region. All rectangular silicon sensors are double-sided with the long strips on the p-side, parallel to and facing the beam axis (z). The short n-side strips along $r - \theta$ are located on the sensor face towards the outside. The slanted sensors are similar, except that the long strips are not exactly parallel to z.

The size of rectangular sensors in the third layer (3.*.* in Fig. 1.10) is 38.4 × 122.8 mm^2 with p-pitch 50 μm at $r - \phi$ side and n-pitch 160 μm at z side. The size of rectangular parallel sensors in layer 4, 5 and 6 is 57.6 × 122.8 mm^2 with p-pitch 75 μm at $r - \phi$ side and n-pitch 240 μm at z side. The size of trapezoidal wedged sensors is 38.4 - 57.6 × 122.8 mm^2 with p-pitch 50 - 75 μm at $r - \phi$ side and n-pitch 240 μm at z side.

The basic data on the VXD are shown in Table 1.1. The structure of VXD is shown in Fig. 1.8. Numbering of VXD layers, ladders and sensors is explained in Fig. 1.9 and Fig. 1.10 [22].

	Layer	*Radius* [mm]	*Ladders*	*Sensors per ladder*	*Sensors*	*Alignment parameters*
PXD	1	14	8	2	16	96
PXD	2	22	12	2	24	144
SVD	3	39	7	2	14	84
SVD	4	80	10	3	30	180
SVD	5	104	12	4	48	280
SVD	6	135	16	5	80	480
Total			65		212	1272

Table 1.1: Number of VXD sensors by layer and ladder

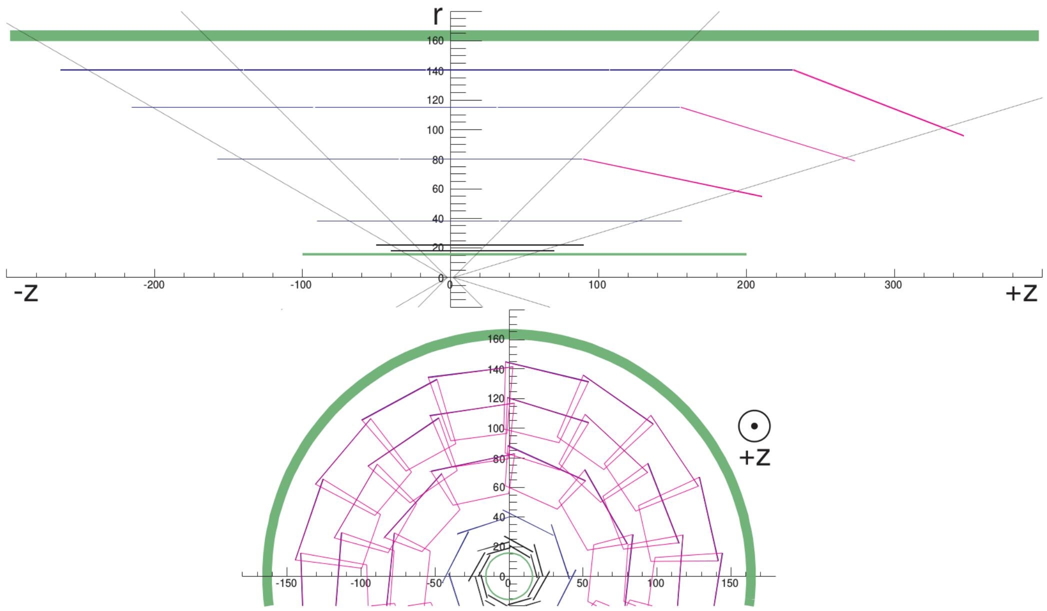

Figure 1.8: *Layout of VXD sensors:* Cross section of VXD in r-z (top) and r-ϕ (bottom) plane. Dimensions are in milimeters.

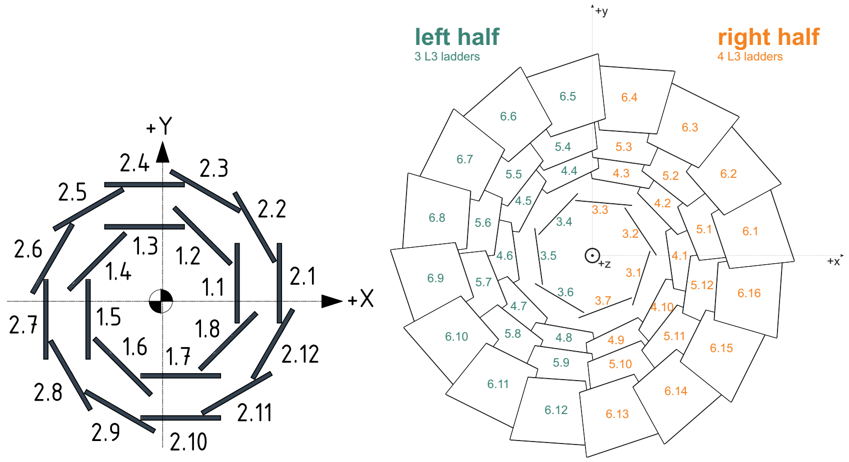

Figure 1.9: *Numbering of VXD ladders:* Layers and ladders of PXD (left) and SVD (right). Numbers are Layer.Ladder.

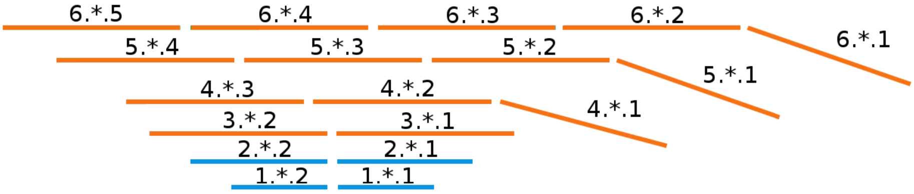

Figure 1.10: *Numbering of VXD sensors:* The first two layers of VXD are **PXD sensors** (blue) and the outer four layer are **SVD sensors** (orange). Numbers are Layer.*.Sensor

1.4 The Central Drift Chamber

The outermost tracking detector is the central drift chamber (CDC). It plays three important roles: reconstruction of tracks, measurement of their momenta and particle identification using energy deposits in the gas volume. It is designed as a hollow cylinder with inner radius of 160 mm and outer radius of 1130 mm. The length of CDC is 2.4 m.

In CDC, there are 14 336 sense and 42 240 field wires in 56 layers. The sense wires are made of tungsten and plated with gold. The diameter of sense wires is 30 μm. The field wires are made of aluminium and their diameter is 126 μm. A layout of wires in layers and a drift cell is shown at Fig. 1.11.

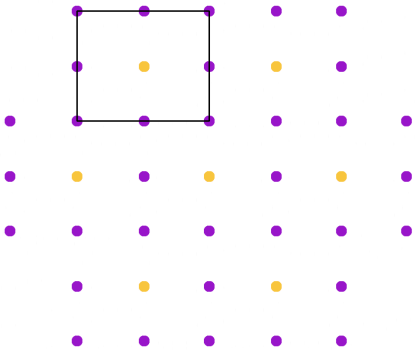

Figure 1.11: Layout of sense (yellow) and field (violet) wires and a **drift cell** (black) [23].

The wires are arranged in superlayers. Each superlayer consists of six layers with the same orientation of wires. A superlayer, which measures the track position in xy plane, is called axial superlayer and the wires of axial superlayer are parallel to the z axis. A stereo superlayer is composed of wires with non-zero angle between sense wires and z axis. The arrangement of the 9 superlayers can be represented as AUAVAUAVA (Fig. 1.12), with axial (A) and stereo superlayers with different angles (U and V). For better resolution the "U" superlayers have positive angle of orientation and "V" superlayers have negative angle.

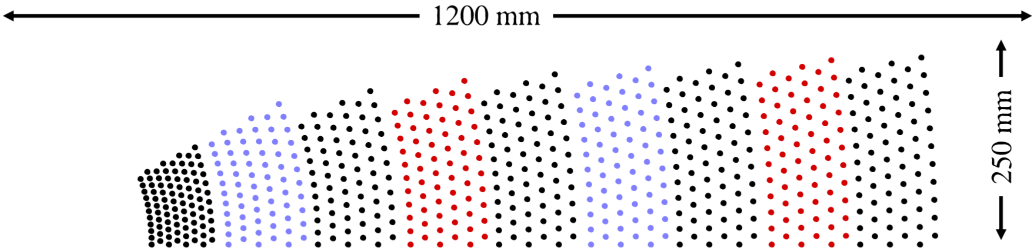

Figure 1.12: *Cross-section of CDC configuration:* The CDC is composed by axial (black), positive stereo (blue) and negative stereo (red) superlayers.

The main structural components of the CDC (Fig. 1.13) are a thin carbon-fiber reinforced plastic (CFRP) inner cylinder, two aluminium endplates and a CFRP outer cylinder. The outer cylinder, with a thickness of 5 mm, supports most of the wire tension of about 4 tonnes. The inner cylinder is about 0.5 mm thin. Tapered aluminium endplates are used for the outer region to reduce the deformation by wire tension. The volume of CDC is filled by a helium-ethane gas mixture. The best choice of gas mixture is 50 % helium and 50 % ethane.

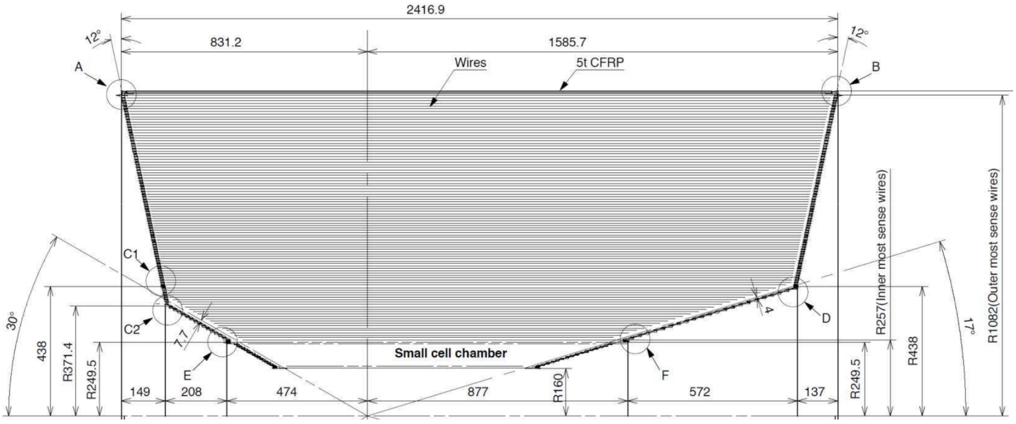

Figure 1.13: *Structure of CDC*

1.5 Detectors for particle identification

For identification of particles we use two different types of detectors. In barrel region, the detection is based on combination of time-of-flight and Cherenkov angle measurements. Incoming charged particles generate Cherenkov radiation in the quartz radiator. The generated photons fly in the volume of radiator and they are detected using an array of photomultipliers. The Cherenkov image is reconstructed from information provided by two coordinates (x, y) and precise timing, which is determined by micro-channel detector at the surfaces of quartz bars. The time of propagation (TOP) counter is composed of 32 quartz bars, each 20 mm × 450 mm × 1250 mm with two bars per module (Fig. 1.14).

In the forward endcap an aerogel ring-imaging cherenkov detector (ARICH) is designed to separate kaons from pions over most of their momentum spectrum and to identify particles below 1 GeV/c. The ARICH (Fig. 1.14) is composed of an aerogel radiator for production of Cherenkov photons, expansion volume for formation of Cherenkov rings, and photon detector. The ARICH consists of 420 modules for detection of photons in seven layers and 248 aerogel tiles of wedge shape in four layers. The inner radius is 56 cm and outer radius is 114 cm [24].

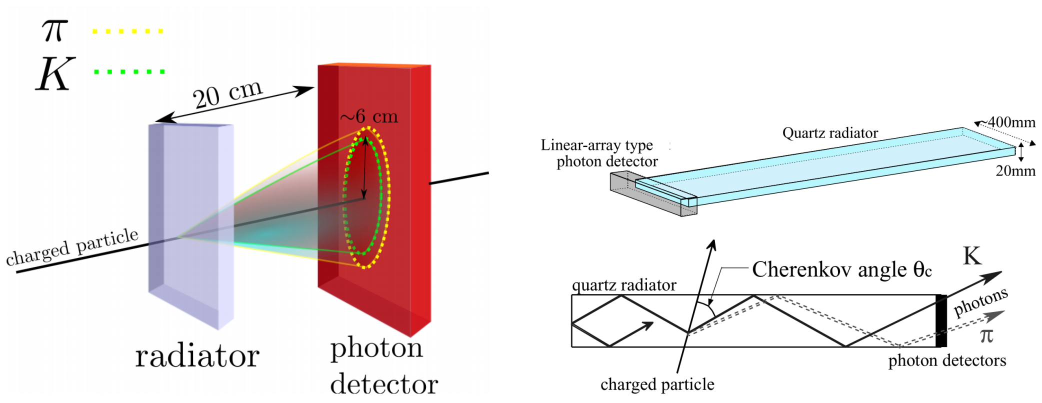

Figure 1.14: *Principles of particle identification detectors:* On the left side is the *ARICH detector*. The yellow Cherenkov ring on the photon detector is generated by pions and the green ring is produced by kaons. The right side shows the *TOP detector* design of a TOP bar (top) and functionality of the TOP detector (bottom).

1.6 The electromagnetic calorimeter

The electromagnetic calorimeter (ECL) is a detector for measurement of energy of electromagnetic particles, detection of neutral particles and luminosity measurement. Very important requirements are high efficiency of photon detection and precise determination of particle energy. The ECL consists of a 3 m long barrel section with an inner radius of 1.25 m and annular endcaps at z = 1.96 m (forward) and z = -1.02 m (backward) from interaction point. The barrel part has a tower structure that projects to a region near the vicinity of the interaction point. It consists of 6624 CsI(Tl) crystals in 29 district shapes. Each crystal is a truncated pyramid of an average size about 6 × 6 cm^2 in cross section and 30 cm in length. The endcaps consists of 2112 CsI crystals of 69 shapes. Photons and electromagnetic particles are detected using electromagnetic cascades. The cascades are accompanied by excitation of scintillator material. These are amplified and detected through photomultipliers mounted at the end of each crystal. The number of photons is directly dependent on the energy deposition of an absorbed particle.

1.7 K_L and muon detector

The last detector of Belle II is a system for detection of long lived kaons and muons. It is composed of 4.7-cm thick metallic plates and active detector elements. The structure of KLM is sandwich-type, the detector is located outside the superconducting solenoid. Because of enough material budget and electromagnetic properties of KLM the K_L can shower hadronically in KLM. In the barrel part there are 15 detector layers and 14 iron plates. 14 sensitive and iron layers are in each endcap (Fig. 1.15).

Resistive plate chambers (RPCs) are composed of two high voltage electrodes and a gas volume between electrodes. Incoming particle generates ion-electrons pairs

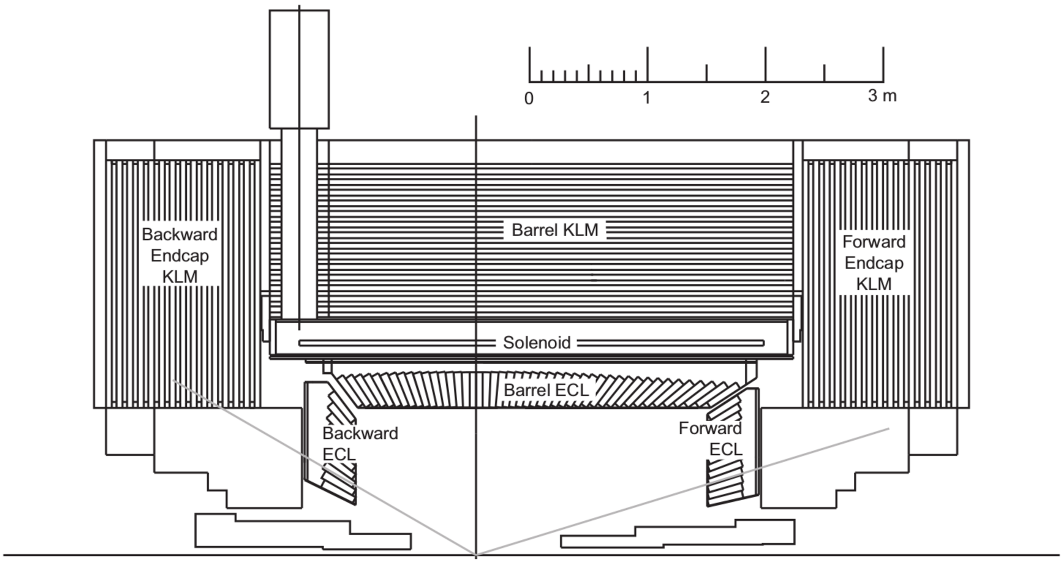

Figure 1.15: *Top parts of KLM and ECL detectors:* The figure shows position detectors to interaction point. In the figure are endcap and barrel parts of CDC or KLM.

in the gas volume that are accelerated by the electric field, producing a streamer between the two electrodes. This streamer is conductive and a voltage drop in the electrodes nearby is produced. The voltage drop is detected by pick-up strip on either side of the chamber.

The muons are detected using their high penetration power to distinguish them from hadrons. The hadrons energy is quickly dissipated through hadronic shower, that is detected by combination of ECL and KLM information. The electron is usually absorbed by the electromagnetic calorimeter. Neutral K_L^0 mesons are able to produce clusters in both ECL and KLM. These clusters are associated with charged tracks in tracking detectors. Clusters without an accompanying charged track are then taken as K_L^0 candidates. Because of the large fluctuations inherent in hadron shower development, the clusters cannot be used to measure K_L^0 energy.

1.8 Trigger

Because of very high luminosity, the Belle II trigger system is very important. The trigger system is focused on several physics processes of interest, measurement of luminosity and calibration of detectors. The trigger is designed for high efficiency for hadronic events, a maximum average trigger rate of 30 kHz, a timing precision of less than 10 ns and a minimum two-event separation of 200 ns.

1.9 Belle II simulation reconstruction software system

The Belle II software system, *basf2* (Belle Analysis and Simulation Framework 2), is based on the ideas from the Belle software system and other experiments such as ILC, LHCb, CDF and Alice [25]. The most common Linux operating systems are supported. The major code is written in C++ 11 and Python scripts are used for run steering. The basf2 is a framework structure with dynamic module loading. Events are processed sequentially by a chain of modules (path). The selection and arrangement of the modules is defined by user in a Python steering file. The set of external libraries is linked to basf2 to provide the necessary function. These include ROOT for storing common data needed for processing of events, Geant4 for full detector simulation, Millepede II package with General broken lines method as calibration and alignment libraries and others.

All the geometry parameter values are stored in the XML format. Currently, geometry definitions are being moved in database and read from there. For simulation, the actual geometry is created using C++ builders from the repository parameters. The software is able to show event display using VGM software.

1.9.1 Monte Carlo simulation

Simulation of Monte Carlo event samples is done in three steps. The first step involves the generation of events for the various physics studies. The physics of B decays and $e^+e^- \to c\bar{c}$ events are simulated by EvtGen and Pythia. A variety of other physics generators are used for various purposes, e.g. dark photon, exotic event generation and cosmic ray events. Particles produced by event generator are fed into the detector simulation.

The second step performs the simulation of the interaction of individual particles passing through the detector, described by all its different materials and geometries, and records the particles' energy deposits in sensitive volumes. The simulation is internally done by Geant4. After the event is processed, it is augmented with created hits, generated trajectories and created secondary particles. The hits are snapshots of physical interaction in sensitive parts of the detector and are saved in hits collections.

The third step simulates the process of signal generation, electronics effects and final detector hit creation. The digitization software performs for each detector component a detailed simulation of in-detector physics process together with electronic effects, taking into account the detector geometry and magnetic field information accessible via the geometry interface. The resulting simulated data can be processed further by the reconstruction modules of each detector component. The simulated information can be used as "truth" information during analysis.

Generation of cosmic rays in the Belle II framework

The Belle II framework uses two different generators of cosmic rays. The older is called "cosmics" [26]. The cosmics is a single muon generator, which is based on the Belle generator. This generator uses acceptance correlations from Belle which cannot be generalized easily.

More advanced studies of cosmic rays can be done using Monte Carlo simulation of proton-induced cosmic-ray cascades in the atmosphere (CRY) [27]. It is used in muon tomography [28], neutrino experiments [29] and development of cosmic shielding materials [30]. The simulation is based on a model of atmosphere and injection of galactic protons. The atmosphere is modelled as a series of 42 constant-density flat layers, each composed of 78% N_2, 21% O_2 and 1% Ar by volume. The top of atmosphere is located at altitude of $\sim$ 31 km. Air density is changed between adjacent layers by 10% with an integrated column density of $\sim$ 1000 g/cm^2. Into the atmosphere are injected galactic protons in the energy range of 1 GeV - 100 TeV (Fig. 1.16).

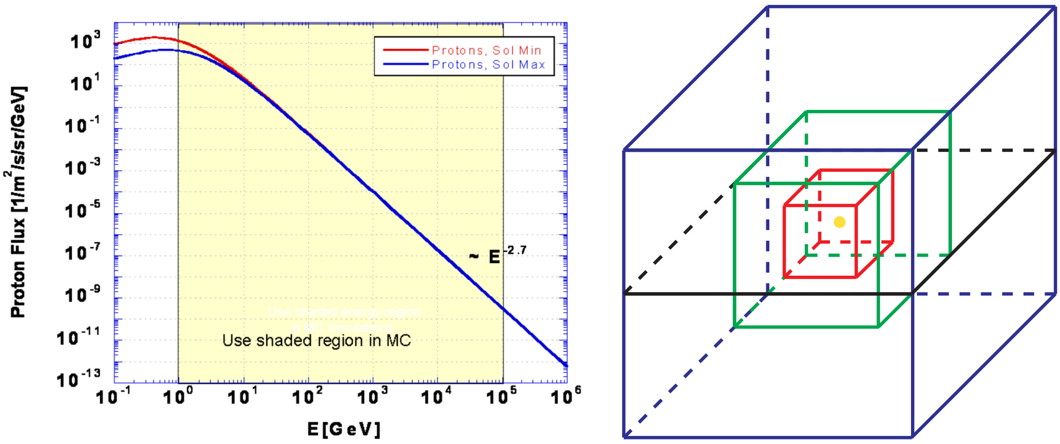

Figure 1.16: *Description of the CRY generator:* Left side shows spectrum of galactic protons incident on the top of the Earth's atmosphere. The CRY generation boxes are explained on the right. There are **global box** (blue), **keep box** (green), **accept box** (red), **generation plane** (black) and **intersection point** (yellow).

For a flux of galactic protons hitting the top of the modelled atmosphere we use the Papini parametrisation:

$$J(E) = A(E+B)^{\alpha}E^{\beta} \qquad protons/m^2/steradian/second/GeV, \tag{1.1}$$

where E is the kinetic energy per nucleon. The values of other parameters are shown in Table 1.2. The proton flux for a specific date $J_{date}(E)$ is a weighted sum of solar minimum $J_{min}(E)$ flux and maximum flux $J_{max}(E)$:

$$J(E)_{date} = (1-x)J_{min}(E) + xJ_{max}(E) \tag{1.2}$$

where $x = |\sin(\pi\Delta T/T_{cycle})|$, T_{cycle} is length of the solar cycle and ΔT is the time (date) since the beginning of the cycle.

	A	B [GeV]	α	β
Solar minimum	18	0.92	-4.00	1.25
Solar maximum	18	1.61	-3.83	1.08

Table 1.2: Values of Papini parametrisation depend to solar status

The generated secondary particles are protons, neutrons, pions, muons, electrons and photons. Because a lot of particles are generated in cosmic showers, the simulation would require a lot of computing time. The authors of CRY developed a system of tables used during the generation. For generation of secondary particles in a specific place on the Earth one needs to define a place of simulation. The generation algorithm can determine elapsed time in the simulation.

The first step of the CRY algorithm is generation of showers from primary particles. After the showers are created, secondary particles are extrapolated into a “generation square” (see Fig. 1.16). In the next step, the algorithm uses particles from the generation square and reconstructs their trajectories in a “global box”. The following conditions are applied for the reconstructed candidates:

- if any particle is in the “accept box”, the event is accepted,
- all particles that are not in a “keep box” are removed.

The keep box should be larger than or the same as the accept box. The generation of cosmic rays has the following settings.

1. *Type of secondary particles:* one can choose between types of particles: *neutrons*, *protons*, *kaons*, *pions*, *muons*, *electrons* and *photons.*
2. *Altitude of place, which we are interested in:* there are three levels available: the sea level, 2.1 or 11.3 kilometers over the sea level.
3. *Latitude of the place that we are interested in:* the generator permits to set the latitude in the latitude range of $(-90°, 90°)$, where the North Pole is defined as having 90°.
4. *Date of the measurement:* this value is connected with the solar cycle.
5. *Kinetic energy threshold for the final particles.*
6. *Sides of the boxes:* as it was explained below, one needs to define three independent boxes.
7. *Side of the generation square:* the setting of plane for the generation of particles.

2. Alignment of vertex detectors

Due to the their proximity to the interaction point, silicon detectors provide accurate information on decay vertices. Silicon detectors can measure points of a track very precisely, but to reconstruct the tracks and vertices in space, we need to know the position of silicon sensors in space very precisely. Actually, the required precision is much higher than what can be achieved during detector installation. In addition, position and shape of silicon sensors can change with time due to variations in ambient temperature and humidity, vibrations, mechanical degrees of freedom etc.

The exact positions of sensors in space must therefore be estimated from tracks, generally speaking, as some linear combinations of tracking residuals. This procedure is called alignment by tracks and has been used to improve tracking precision in all major experiments, including Belle.

2.1 Track based alignment

The alignment task is to find correction to nominal positions of sensors. To estimate these parameters, we use a large set of tracks, and use the degrees of freedom remaining after track fits to estimate the alignment parameters. Table 1.1 shows number of alignment parameters for the Belle II VXD. The number is large, and so we have a large problem to solve. To make things more complicated, common experience shows that even a large number of tracks used to estimate alignment parameters does not guarantee a good result: unless we have a rich set of tracks of several different types, we may end up with a number of linear combinations of alignment parameters that cannot be estimated from the given set of tracks. Such combinations are called "χ^2 invariant modes". To find good alignment we have to impose constraints on alignment parameters or use a richer set of tracks.

2.2 Alignment algorithm

The normalized tracking residuals are [31]:

$$z_{ij} = \frac{u_{ij}^m - u_{ij}^p(\boldsymbol{\tau}_j, \boldsymbol{a})}{\sigma_{ij}} = \frac{r_{ij}(\boldsymbol{\tau}_j, \boldsymbol{a})}{\sigma_{ij}}, \tag{2.1}$$

where u_{ij}^m is a recorded measurement of hit i on the track j, u_{ij}^p is predicted measurement from track model dependent on track parameters $\boldsymbol{\tau}_j$ and alignment parameters $\boldsymbol{a}$, σ_{ij} is the uncertainty of measurement and r_{ij} is a single residual.

We find optimum track and alignment parameters by minimizing the joint χ^2:

$$\chi^2(\boldsymbol{\tau}, \boldsymbol{a}) = \sum_j^{tracks} \sum_i^{hits} z_{ij}^2(\boldsymbol{\tau}_j, \boldsymbol{a}). \tag{2.2}$$

The result of alignment algorithm is a solution with the smallest χ^2-function. All single tracks and vertex constrained decays reconstructed in the tracking system can be used for alignment.

2.2.1 Millepede II

Millepede II is based on global linear χ^2 minimization with constraints. This method starts with linearisation of the normalized residuals z_{ij} in the χ^2 function [32]:

$$\chi^2(\boldsymbol{\tau},\boldsymbol{a}) = \sum_{j}^{tracks}\sum_{i}^{hits} z_{ij}^2(\boldsymbol{a},\boldsymbol{\tau}_j) \simeq \sum_{j}^{tracks}\sum_{i}^{hits} \frac{1}{\sigma_{ij}^2}(r_{ij}(\boldsymbol{\tau}_j^0,\boldsymbol{a}^0) + \frac{\partial r_{ij}}{\partial \boldsymbol{a}}\delta\boldsymbol{a} + \frac{\partial r_{ij}}{\partial \boldsymbol{\tau}_j}\delta\boldsymbol{\tau}_j)^2, \tag{2.3}$$

where $\boldsymbol{\tau}_j^0, \boldsymbol{a}^0$ are initial estimates of the geometry and track parameters, $\delta\boldsymbol{\tau}_j$ and $\delta\boldsymbol{a}$ are small corrections. Track parameters are specific to the particular track and are called local parameters. Alignment parameters are common to the whole set of tracks and are therefore called global parameters.

Minimization of $\chi^2(\boldsymbol{\tau},\boldsymbol{a})$ is equivalent to solving a system of linear equations. The number of global parameters depends on the number of used detectors. The number of local parameters is fundamentally larger. The matrix of the resulting system has a specific structure:

$$\begin{pmatrix} \sum \boldsymbol{C}_j & \dots & \boldsymbol{G}_j & \dots \\ \vdots & \ddots & 0 & 0 \\ \boldsymbol{G}_j^T & 0 & \Gamma_j & 0 \\ \vdots & 0 & 0 & \ddots \end{pmatrix} \begin{pmatrix} \boldsymbol{a} \\ \vdots \\ \delta\tau_j \\ \vdots \end{pmatrix} = \begin{pmatrix} \sum \boldsymbol{b}_j \\ \vdots \\ \beta_j \\ \vdots \end{pmatrix}. \tag{2.4}$$

The derivatives of residuals with respect to local parameters are included in submatrices $\boldsymbol{\Gamma}$ and the derivatives with respect to global parameters are found in the matrices $\boldsymbol{C}_j$. The matrices $\boldsymbol{G}_j$ are composed of combinations of global and local derivatives. The vector $\boldsymbol{b}$ includes product of global derivatives and the normalized residuals and $\boldsymbol{\beta}_j$ local derivatives and the normalized residuals. The solution of 2.4 can be reduced to a smaller equation system for the alignment parameters $\boldsymbol{a}$ by Schurr decomposition:

$$\boldsymbol{C}'\boldsymbol{a} = \boldsymbol{b}', \tag{2.5}$$

where $\boldsymbol{C}'$, $\boldsymbol{b}'$ are:

$$\boldsymbol{C}' = \sum_i \boldsymbol{C}_i - \sum_i \boldsymbol{G}_i \boldsymbol{\Gamma}_i^{-1}\boldsymbol{G}_i^T \qquad \boldsymbol{b}' = \sum_i \boldsymbol{b}_i - \sum_i \boldsymbol{G}_i(\boldsymbol{\Gamma}_i^{-1}\boldsymbol{\beta}_i). \tag{2.6}$$

Using the reduced matrix 2.5 to solve the alignment problem is the core idea of the Millepede algorithm. Using this idea the correction of parameters for each track $\delta\boldsymbol{\tau}_j$ and correction of alignment parameters $\delta\boldsymbol{a}$ are calculated:

$$\delta\boldsymbol{\tau}_j = \boldsymbol{\Gamma}_j^{-1}\boldsymbol{\beta}_j \qquad \delta\boldsymbol{a} = (\boldsymbol{C}')^{-1}\boldsymbol{b}'. \tag{2.7}$$

To reduce of degrees freedom of the solution the problem can be extended to include a set of linear constraints. Millepede internally use Gaussian elimination to reduce additional equations.

2.2.2 Alignment parametrization

We use two different coordinates systems for description of measurements. The first is the global laboratory frame (Fig. 2.1). For every detector we define its local frame of measurement, which is defined by u, v, w coordinates. The w is perpendicular to the sensor plane and u and v have directions along the sides of sensor planes (Fig. 2.1) with origin at sensor's center. In the local frame and need to be transformed to the global system. The vector in the local frame is defined as $\mathbf{q} = (u, v, w)$, the vector in global system is expressed $\mathbf{r} = (x, y, z)$. The transformation from the global to local system is [33]:

$$\mathbf{r} = \mathbf{R}^T \mathbf{q} + \mathbf{r}_0, \tag{2.8}$$

where $\mathbf{r_0} = (x_0, y_0, z_0)$ is the position of sensor center in the global system and $\mathbf{R}$ is a rotation matrix. The alignment procedure determines a correction to initial transformation as an incremental rotation $\Delta\mathbf{R}$ and a translation $\Delta\mathbf{q} = (\Delta u, \Delta v, \Delta w)$. The transformation equation 2.8 is extended to:

$$\mathbf{r} = \mathbf{R}^T \Delta\mathbf{R}(\mathbf{q} + \Delta\mathbf{q}) + \mathbf{r}_0. \tag{2.9}$$

The rotation correction $\Delta\mathbf{R} = \mathbf{R}_\gamma \mathbf{R}_\beta \mathbf{R}_\alpha$ is expressed as a product of small rotations $\mathbf{R}_\alpha$, $\mathbf{R}_\beta$ and $\mathbf{R}_\gamma$ by $\Delta\alpha$, $\Delta\beta$, $\Delta\gamma$ around the u-axis, the new v-axis and new w-axis (Fig. 2.1). The translation corrections and rotation angles compose alignment parameters for a single planar sensor $\mathbf{a} = (\Delta u, \Delta v, \Delta w, \Delta\alpha, \Delta\beta, \Delta\gamma)^T$.

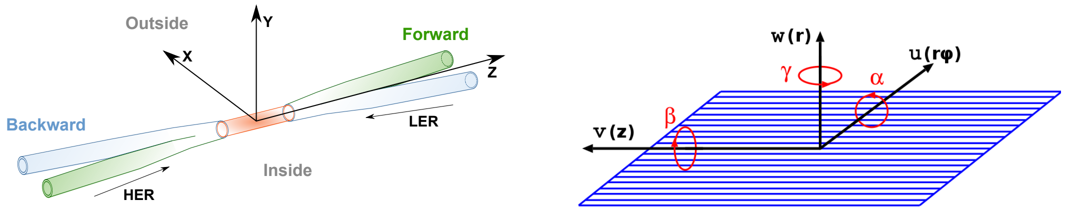

Figure 2.1: *The experiment coordinate system:* the global coordinate system (left) and a local sensor coordinate system (right)

2.2.3 Track parametrization

The trajectory of a charged particle propagating in vacuum with a constant magnetic field is a helix with five parameters. Energy loss in the detector material due to ionization or radiation leads to a reduction of the momentum. Multiple scattering, mainly due to Coulomb interaction with nuclei in the atoms, results in changes in direction and spatial position.

General broken lines

The general broken lines (GBL) [34] method is a fast global track refit adding the description of multiple scattering to an initial trajectory. Any material distribution can be described as a thick scatterer, imposing a change of direction and displacement to the particle trajectory. A thick scatterer can be equivalently described by two thin scatterers, which only change the variance of change of direction, at proper positions. The required propagation from a measurement plane or scatterer to the previous and next scatterer is using a locally linearised track model. This linearisation may necessitate iterations of the fitting procedure.

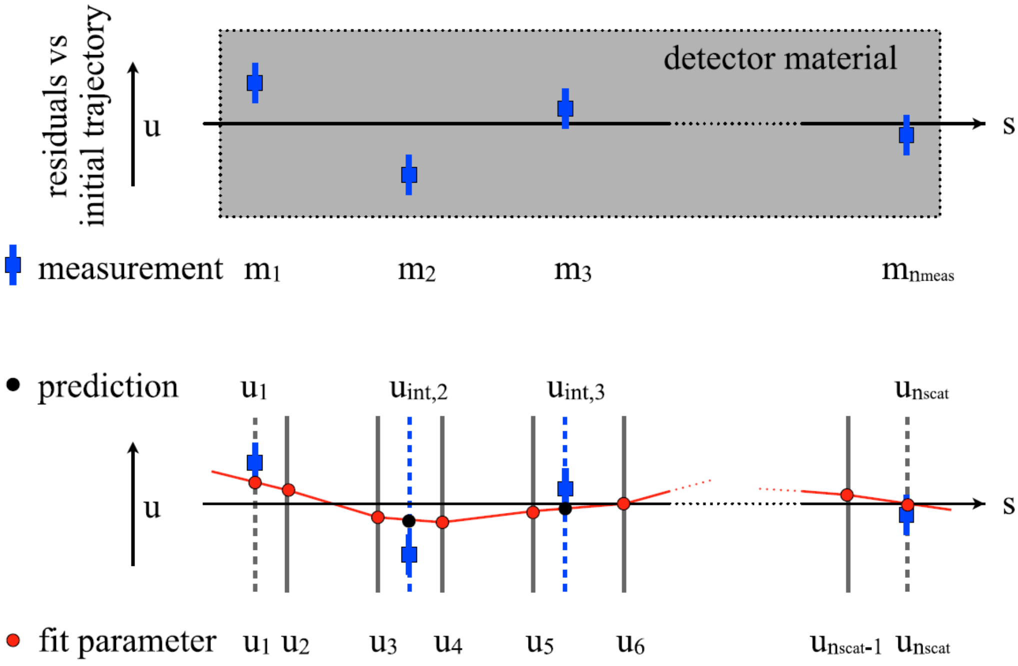

Figure 2.2: *Explanation of GBL method* using a simple example: Residuals versus initial trajectory (top) and broken lines trajectory based on thin scatterers (bottom). The material between measurement i and $i+1$ is described with two thin scatterers. The fit prediction $u_{int,i}$ for measurement m_i is obtained by interpolation between the enclosing scatterers [35].

In the local coordinate system a track is defined using slopes and offsets as $(q/p, \frac{du}{dw}, \frac{dv}{dw}\ , u, v)$, where q/p is inverse momentum. A fit parameters of track, which traverses n_{scat} thin scatterers, can be expressed as $\mathbf{x} = (\Delta q/p, \mathbf{u}_1, ..., \mathbf{u}_{scat})$. The correction to the track parameter at each thin scatterer i is $\Delta\mathbf{p}_{loc} = (\Delta q/p, \mathbf{u}'_i, \mathbf{u}_i)$. At measurement planes the track parameter correction $(\Delta q/p, \mathbf{u}'_{int}, \mathbf{u}_{int})$ can be obtained from interpolation between the enclosing scatterers. At each local system $\Delta\mathbf{p}_{loc}$ is affected only by $\Delta p/q$ and two adjacent offsets. Multiple scattering kinks are defined by triplets of thin scatterers.

The covariance matrix $\mathbf{V}_k$ of the multiple scattering kinks $\mathbf{k}$ in the local system can be calculated from the variance θ_0^2. The slope variance θ_0^2 is calculated during extrapolation in detector geometry together with propagation Jacobians. The matrix $\mathbf{V}_k$, which is composed of projections $c_{u,v} = \mathbf{e}_{track} \cdot \mathbf{e}_{u,v}$ of offset directions $\mathbf{e}_{u,v}$ onto the track direction $\mathbf{e}_{track}$, is:

$$\mathbf{V}_k = \frac{\theta_0^2}{(1 - c_u^2 - c_v^2)^2} \begin{pmatrix} 1 - c_v^2 & c_u c_v \\ c_v c_u & 1 - c_u^2 \end{pmatrix} \tag{2.10}$$

The trajectory should be iterated, if the resulting fit parameters are not small corrections as assumed for linearisation. With already estimated non zero values of kinks in $\mathbf{k}_0$: $\mathbf{k}(\mathbf{x}) = \mathbf{H}_k\mathbf{x} + \mathbf{k}_0$. The expected value is $\langle \mathbf{k}(\mathbf{x}) \rangle = \mathbf{0}$, where $\mathbf{H}_k = \frac{\partial \mathbf{k}}{\partial \mathbf{x}}$ and $\mathbf{k}_i = \mathbf{u}'_{i+1} - \mathbf{u}'_{i-1}$.

The measurements $\mathbf{m}$ are the residuals with respect to the initial trajectory (r_{ij} at 2.1). It is the comparison of observables with predictions of local track parameters in the measurement plane. The linearised prediction is $\mathbf{m}(\mathbf{x}) = \mathbf{H}_m\mathbf{x}$, where $\mathbf{H}_m = \frac{\partial \mathbf{u}_{int}}{\partial \mathbf{x}}$. If covariance matrices $\mathbf{V}_m$ are not diagonal, they will be diagonalised automatically.

The fit parameters are determined by minimisation of χ^2 function:

$$\chi^2(\mathbf{x}) = \chi^2_{meas}(\mathbf{x}) + \chi^2_{scat}(\mathbf{x}). \tag{2.11}$$

The part from measurement is:

$$\chi^2_{meas}(\mathbf{x}) = \sum_{i=1}^{n_{meas}} (\mathbf{H}_{m,i}\mathbf{x} - \mathbf{m}_i)^T \mathbf{V}^{-1}_{m,i} (\mathbf{H}_{m,i}\mathbf{x} - \mathbf{m}_i) \tag{2.12}$$

and the scattering part is:

$$\chi^2_{scat}(\mathbf{x}) = \sum_{i=2}^{n_{scat}-2} (\mathbf{H}_{k,i}\mathbf{x} + \mathbf{k}_{0,i})^T \mathbf{V}^{-1}_{k,i} (\mathbf{H}_{k,i}\mathbf{x} + \mathbf{k}_{0,i}). \tag{2.13}$$

The complete linear equation $\mathbf{A}\mathbf{x} = \mathbf{b}$ is composed of a bordered band matrix $\mathbf{A}$ with size n depending on the number of scatterers, band width m and border size 1 in presence of magnetic field. The matrix is built from the propagation Jacobians between local systems on the initial trajectory.

3. Generation and properties of alignment datasets

Our alignment study is focused on solving the alignment problem for the vertex detection system of Belle II. The study uses all 1272 alignment parameters (See Table 1.1). To reduce the degrees of freedom we use a set of simple constraints. *We require that the sum of alignment corrections per each rigid body parameter (projected to global system) is zero.* Each run starts with sensors, layers and ladders at ideal position. In this study we generate track samples using three different generators: cosmic rays, $\Upsilon(4S)$ resonance and muon pairs. We want to know the convergence properties of the alignment procedure for the three samples and optimal "mixture" giving the best residual alignment. The alignment study consists of several parts. For all physical processes we start with convergence studies. The result of convergence studies is used for discussion of alignment results.

3.1 Convergence study

3.1.1 Building alignment samples

We generate 20 independent blocks containing on average 60 000 ± 15 000 alignment records (tracks). The blocks are then cumulatively merged to create a sequence of samples increasing linearly in size. To compose mixture samples, we alternate the blocks appropriately. The blocks were generated in nominal geometry, no misalignment was applied. For each sample, we calculate the mean deviation (bias) of each alignment parameter and standard deviation from 10 independent runs. The mean of alignment parameters is an estimate of the parameter's bias.

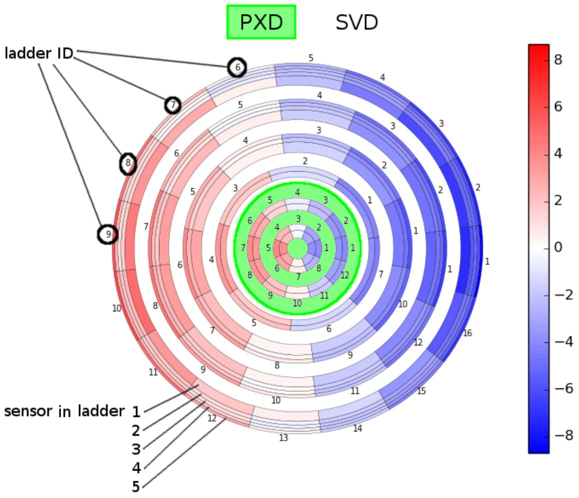

Figure 3.1: *The arrangement of ring plot:* All sensors, ladders and six layers of VXD are arranged in a ring plot. The color bar is on the right.

The pattern of biases and standard deviations for all VXD sensors can be conveniently visualised using a "ring plot" (Fig. 3.1). A ring plot is a map of a quantity over all 212 VXD sensors, and roughly reproduces the topology of the VXD (layer/ladder/sensor), so that the correspondence is intuitive. Six ring plots are needed to display all alignment parameters for the VXD.

The analysis is based on Monte Carlo information (no hit reconstruction). To pass for analysis, a track must have 5 to 24 hits in the VXD, and quality of the track fit at least 0.001.

3.2 The $\Upsilon(4S)$ dataset

This data set is composed of randomly generated events from the $\Upsilon(4S)$ resonance. Typically an event contributes 8 tracks. The convergence result for the first ladder in first layer is shown in Fig. 3.3 and for the first ladder in sixth layer is in Fig. 3.4. The six ring plots of biases are shown in Fig. 3.2.

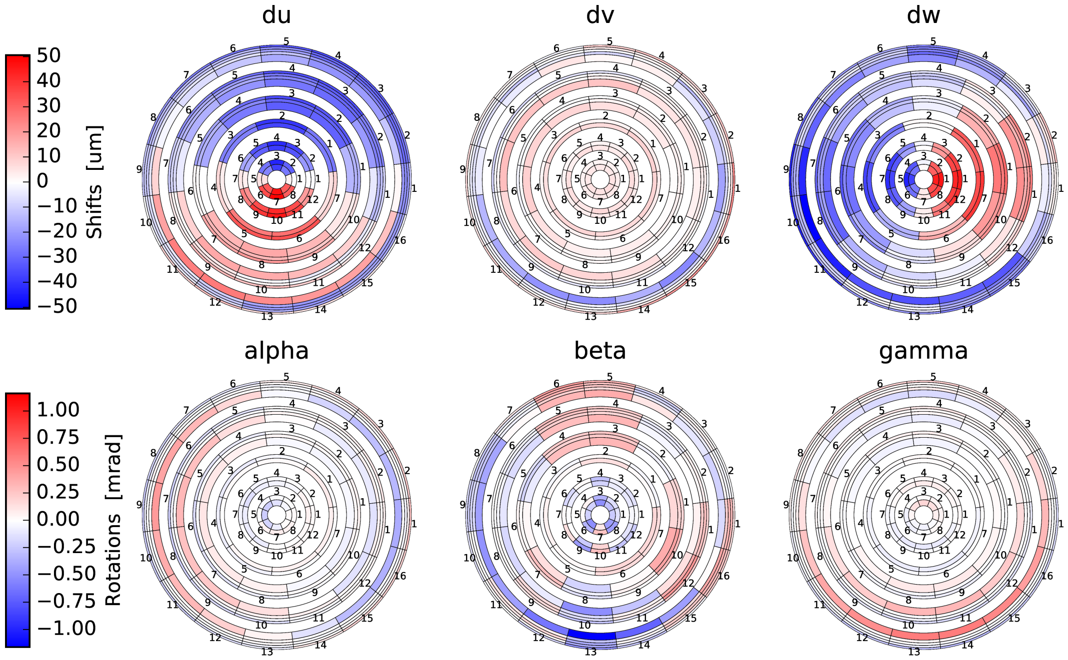

Figure 3.2: *The sixplots of biases for the* $\Upsilon(4S)$ *dataset:* The calculated alignment parameters are based on 1 200 000 records of $\Upsilon(4S)$ dataset. The color bars are shown on the left side. For translation in du we can see symmetrical pattern and very similar pattern for translation in dw. Running alignment on ideal geometry, we ended up with a large residual misalignment, with translation up to 50 μm and rotation up to 1 mrad. We also see that the deviations are organized in distinctive patterns.

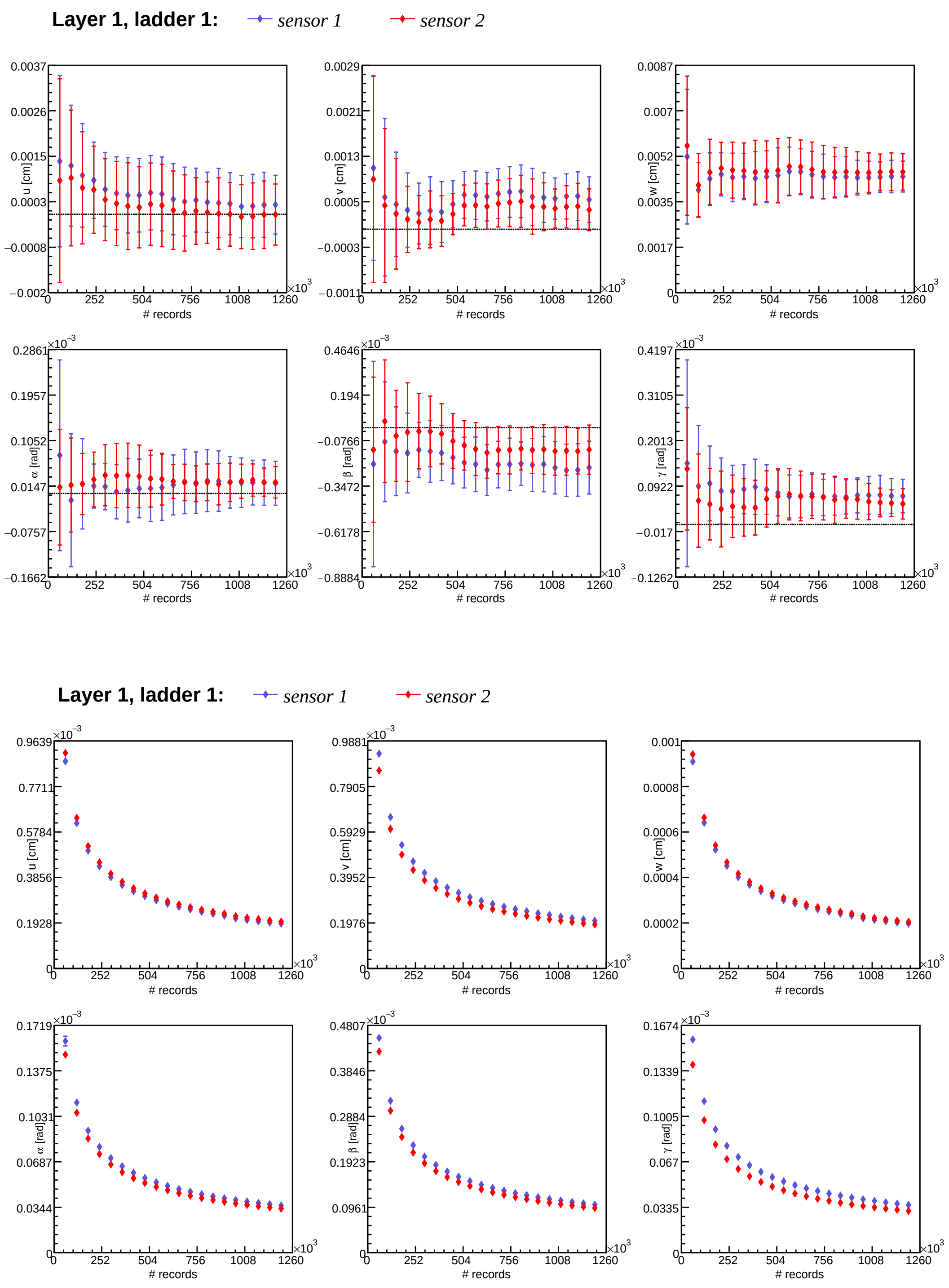

Figure 3.3: *The convergence study of the* $\Upsilon(4S)$ *dataset for mean and standard deviation calculated by the Millepede algorithm:* The top half shows means for each alignment parameter. The dotted line shows ideal alignment. The standard deviations of alignment parameters are shown in the bottom half. As can be seen (most clearly in the plots on the right), the algorithm converges quite fast, but not necessarily to the correct (zero) value.

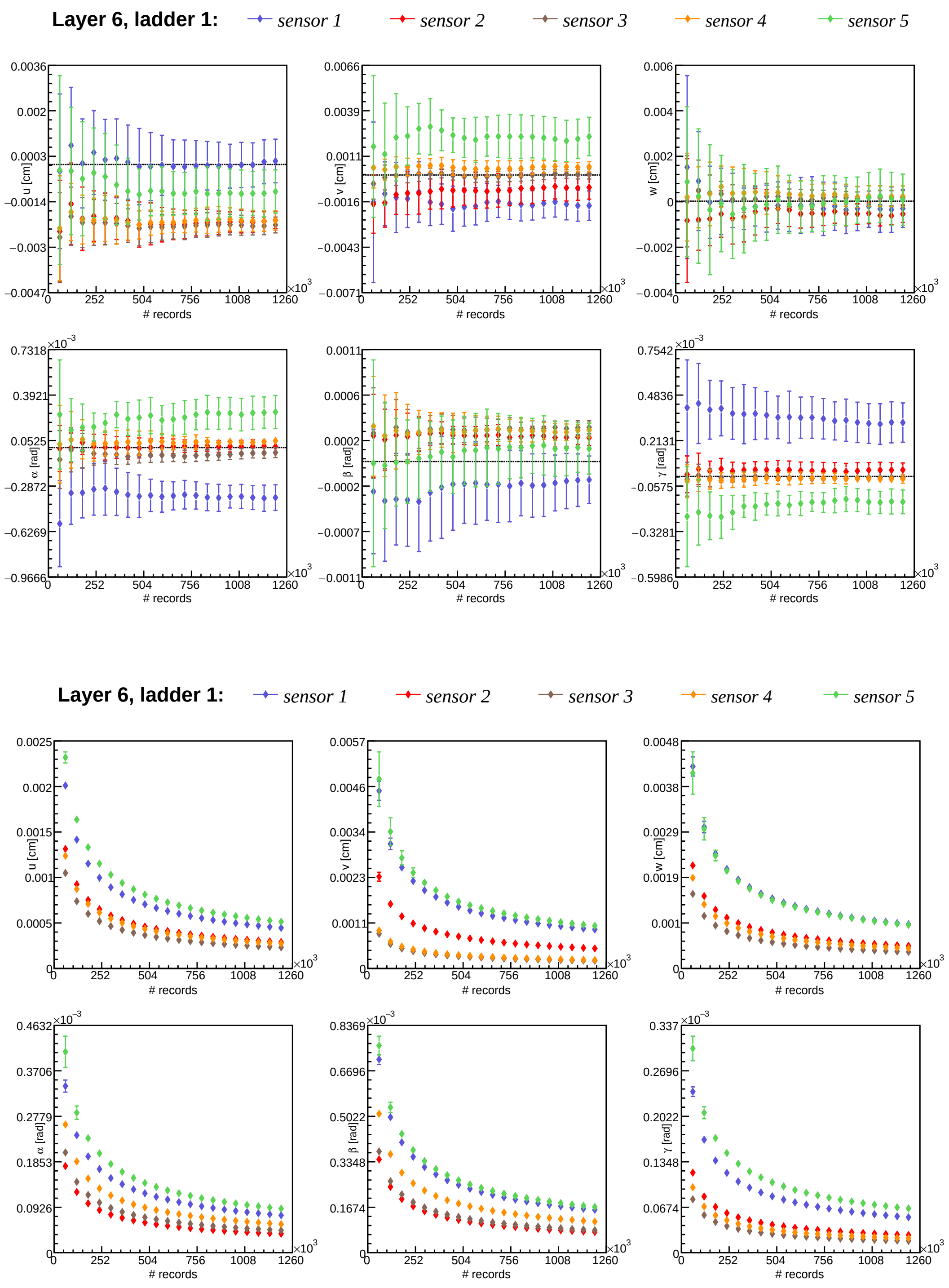

Figure 3.4: *The convergence study of the* $\Upsilon(4S)$ *dataset for mean and standard deviation calculated by the Millepede algorithm:* The top half shows means for each alignment parameter. The dotted line shows ideal alignment. The standard deviations of alignment parameters are shown at bottom half. As can be seen, the algorithm converges quite fast, but not necessarily to the correct (zero) value.

3.3 Cosmic rays

The cosmic muon tracks are an important source for alignment. Their trajectories connect distant parts of the detector. The cosmic rays, which can be reconstructed as straight lines if magnetic field is not present, were used as an important element of alignment of other experiments in high energy physics experiments [31] [36] [37].

The cosmic muons were generated by the Cosmics generator. The convergence result for the first ladder in first layer is shown in Fig. 3.6 and for the first ladder in sixth layer is in Fig. 3.7. The six ring plots of biases are shown in Fig. 3.5.

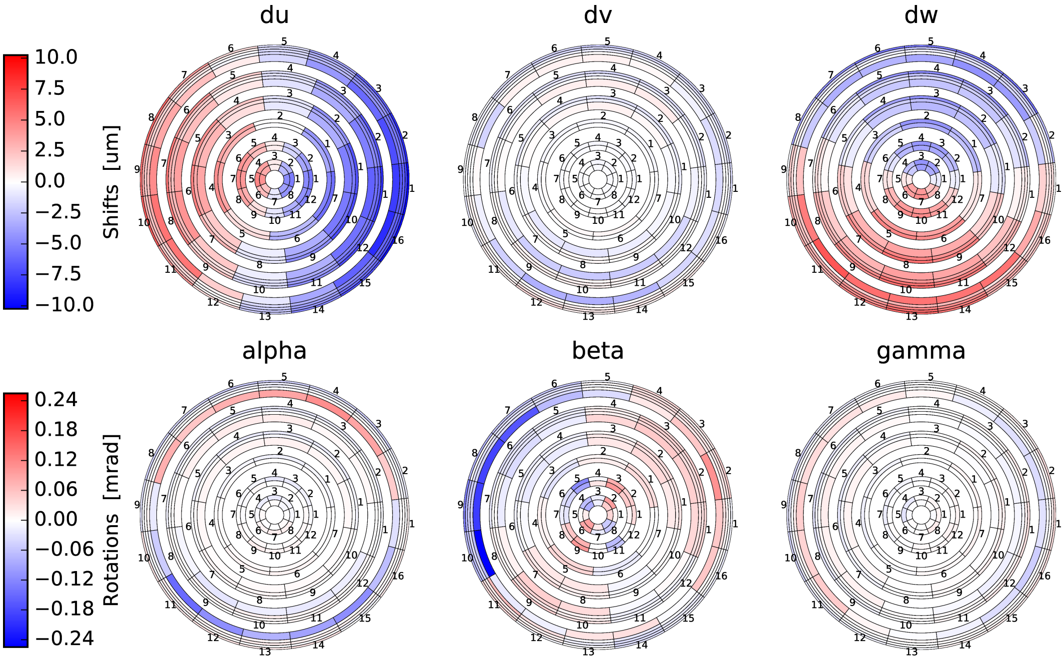

Figure 3.5: *The sixplots of biases for cosmic dataset:* The calculated alignment values are based on 1 200 000 records of the cosmic dataset. The color bars are shown on the left. The alignment using the cosmic dataset is more precise than that for the $\Upsilon(4S)$ dataset. The ranges are 10 μm (as compared to 50 μm for $\Upsilon(4S)$) and 0.24 mrad (vs. 1 mrad). However, the residual patterns are seen again, the symmetric pattern for u and w translation.

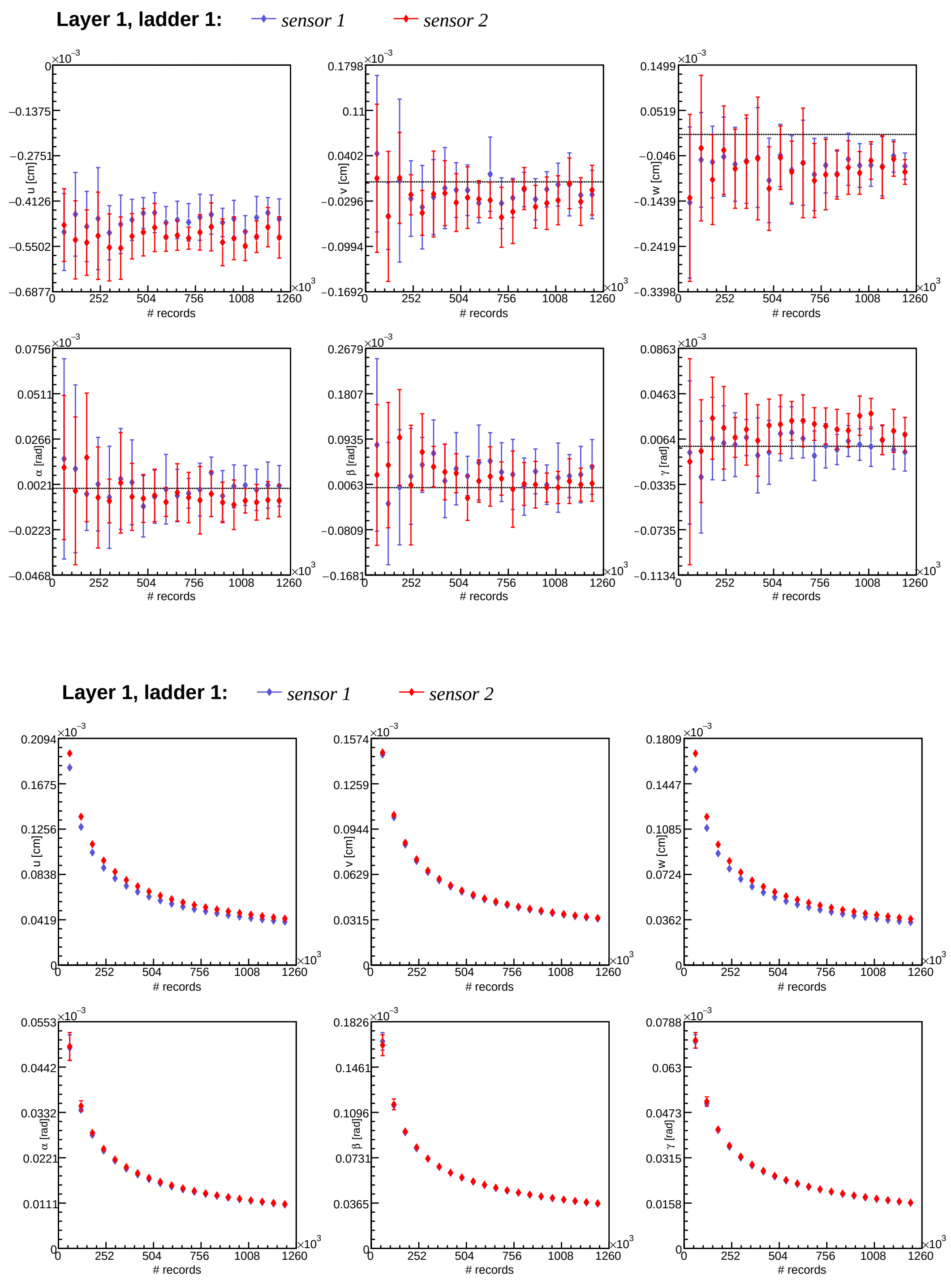

Figure 3.6: *The convergence study of the cosmic dataset for mean and standard deviation calculated by the Millepede algorithm:* The top half shows means for each alignment parameter. The dotted line shows ideal alignment. The standard deviations of alignment parameters are shown in bottom half. As can be seen (most clearly in the plots on the left), the algorithm converges quite fast, but not necessarily to the correct (zero) value.

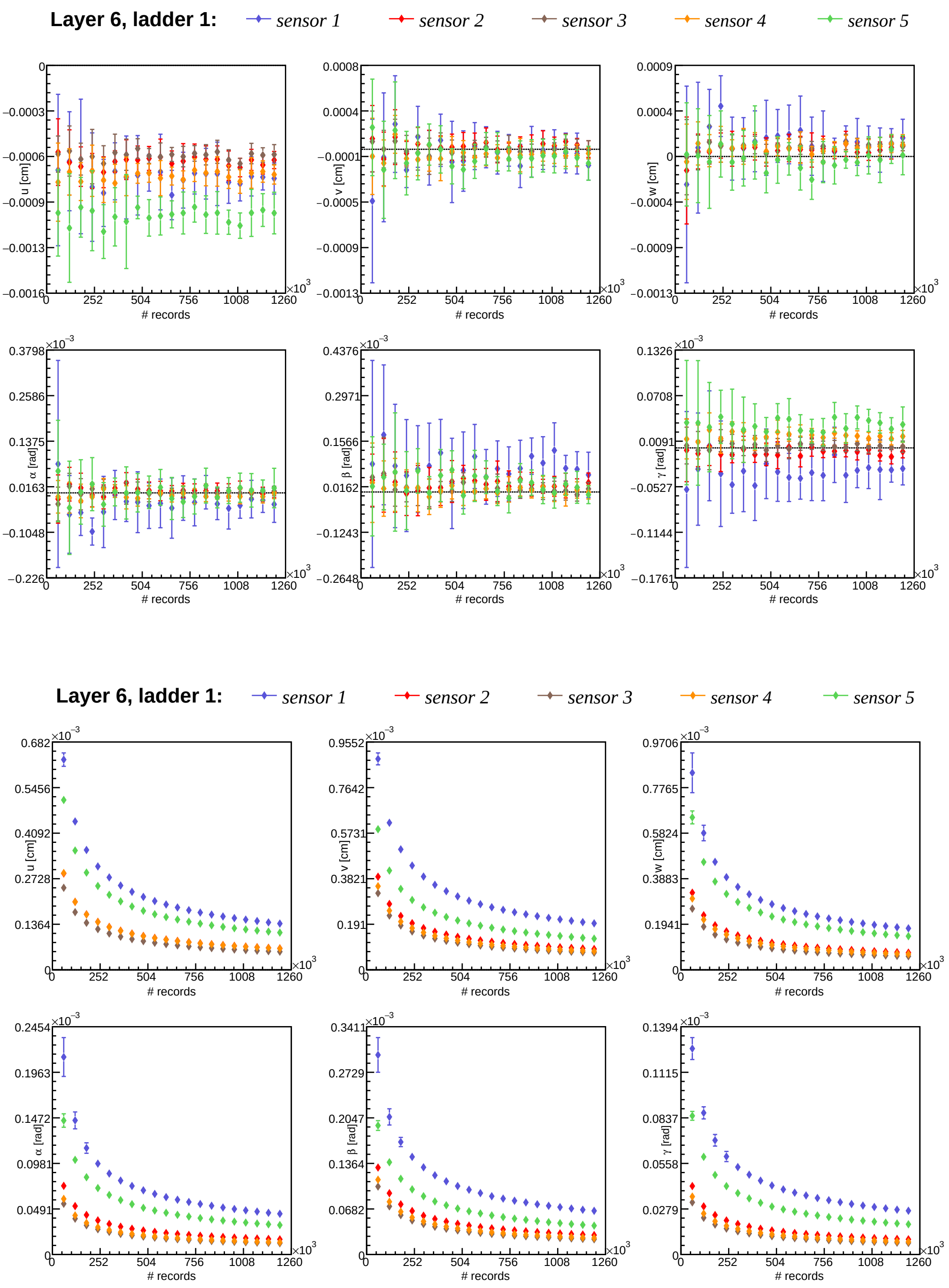

Figure 3.7: *The convergence study of the cosmic dataset for mean and standard deviation calculated by the Millepede algorithm:* The top half shows means for each alignment parameter. The dotted line shows ideal alignment. The standard deviations of alignment parameters are shown in bottom half. As can be seen (most clearly in the plots on the left), the algorithm converges quite fast, but not necessarily to the correct (zero) value.

3.4 Muon pairs

Our last dataset was composed of muon pairs from the process $e^+e^- \to \mu^+\mu^-$. This dataset is a very specific process. Both tracks can be assumed to originate from the same point, vertex. Instead of doing two independent fits for parameters of each of those tracks $\mathbf{x}_{\mu^+}, \mathbf{x}_{\mu^-}$ we use a fit for combined object with parameters $\mathbf{x}_{\mu\mu} = (\mathbf{x}_{\mu^+}, \mathbf{x}_{\mu^-}, \boldsymbol{\omega})$, where $\boldsymbol{\omega}$ is an optional set of additional parameters such as a position of the common vertex. Those parameters can contribute to the χ^2 of combined track, where the contribution takes similar form as in Eq. 2.12 and Eq. 2.13:

$$\chi^2_\omega(\mathbf{x}) = (\mathbf{H}_\omega \mathbf{x})^T \mathbf{V}_\omega^{-1} (\mathbf{H}_\omega \mathbf{x}). \tag{3.1}$$

We refer to this decay as "vertex constraint decays". The covariance matrix V_ω is provided by the framework from the parameters of the primary beam spot.

The convergence result for the first ladder in first layer is shown in Fig. 3.9 and for the first ladder in sixth layer is in Fig. 3.10. The six ring plots of biases are shown in Fig. 3.8.

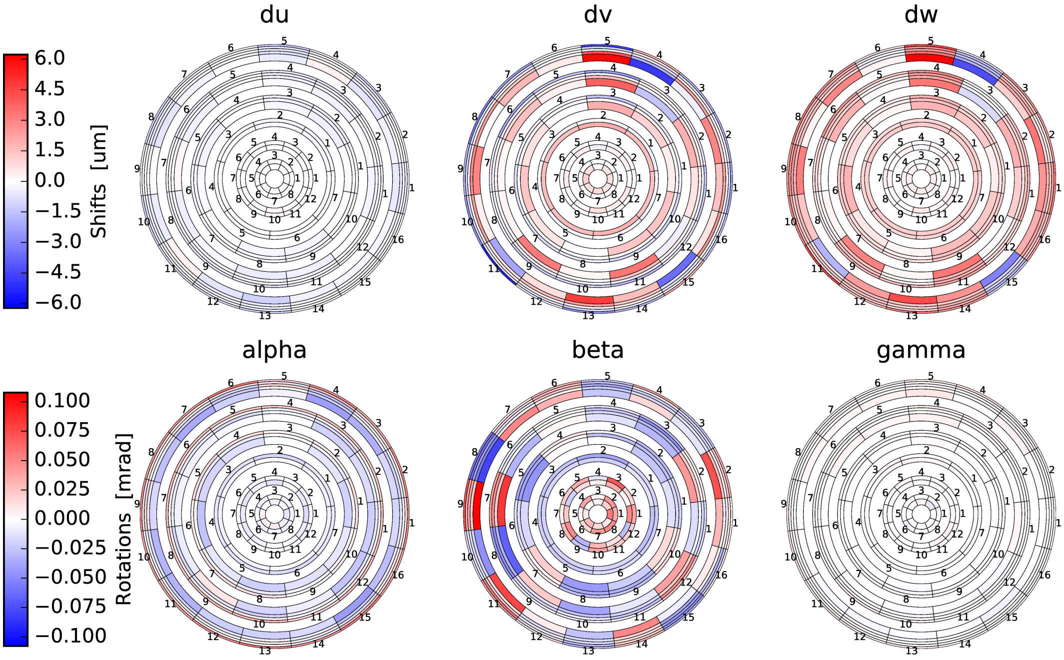

Figure 3.8: *The sixplots of biases for the muon pairs dataset:* The calculated alignment parameters are based on 1 200 000 records of the muon pairs dataset. The color bars are shown at left side. The ranges of shifts and rotations are very similar to the cosmic dataset. γ and u parameters are determined more preciously than others. The patterns observed for cosmic or $\Upsilon(4S)$ datasets are not present, and the distribution of u, w, β is nearly normal. However, we see a symmetrical pattern for α parameter, but it is different than in for other datasets.

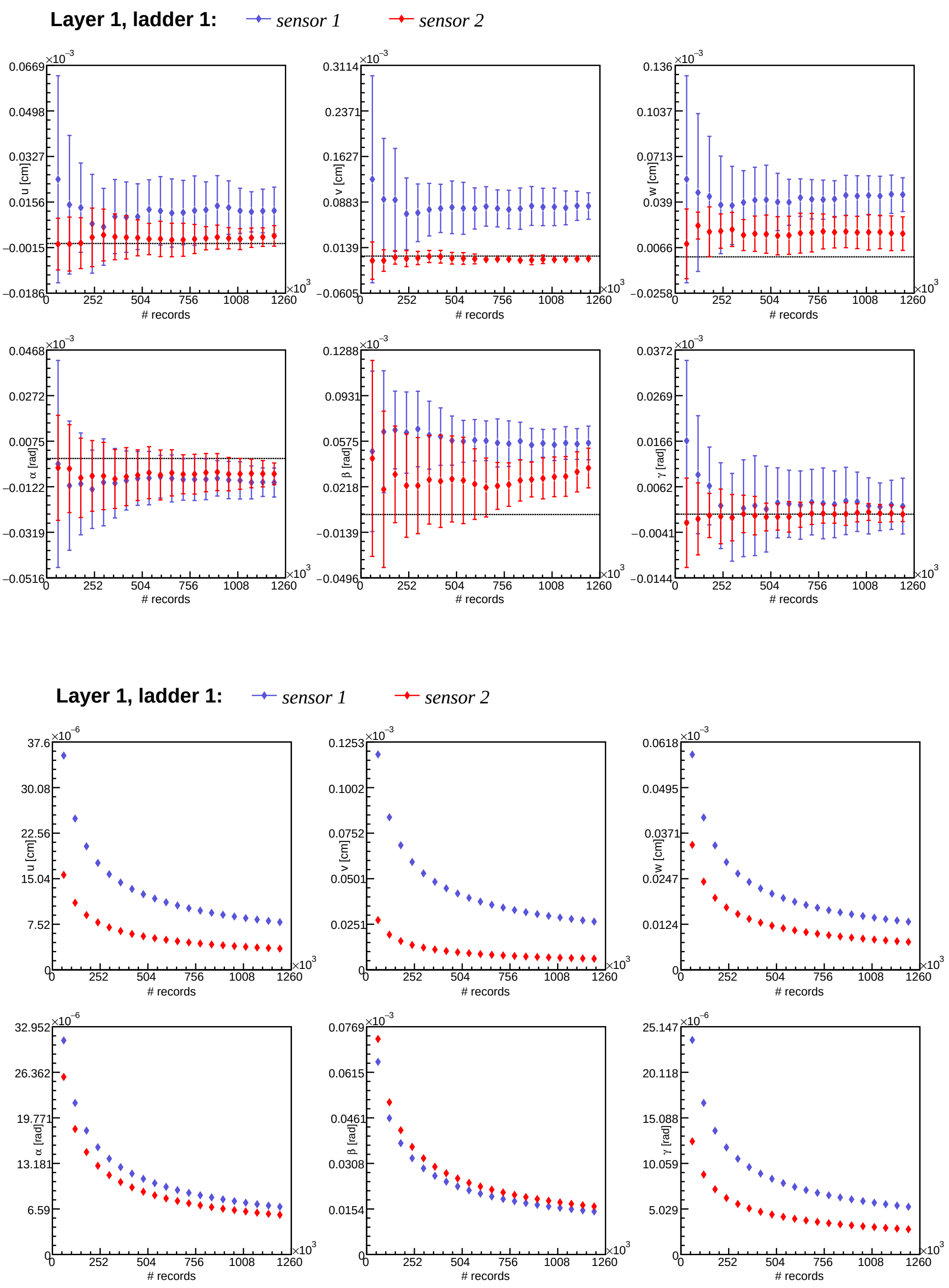

Figure 3.9: *The convergence study of the muon pairs dataset for mean and standard deviation calculated by the Millepede algorithm:* The top half shows means for each alignment parameter. The dotted line shows ideal alignment. The standard deviations of alignment parameters are shown in bottom half. As can be seen (most clearly in the plots on the left), the algorithm converges quite fast, but not necessarily to the correct (zero) values.

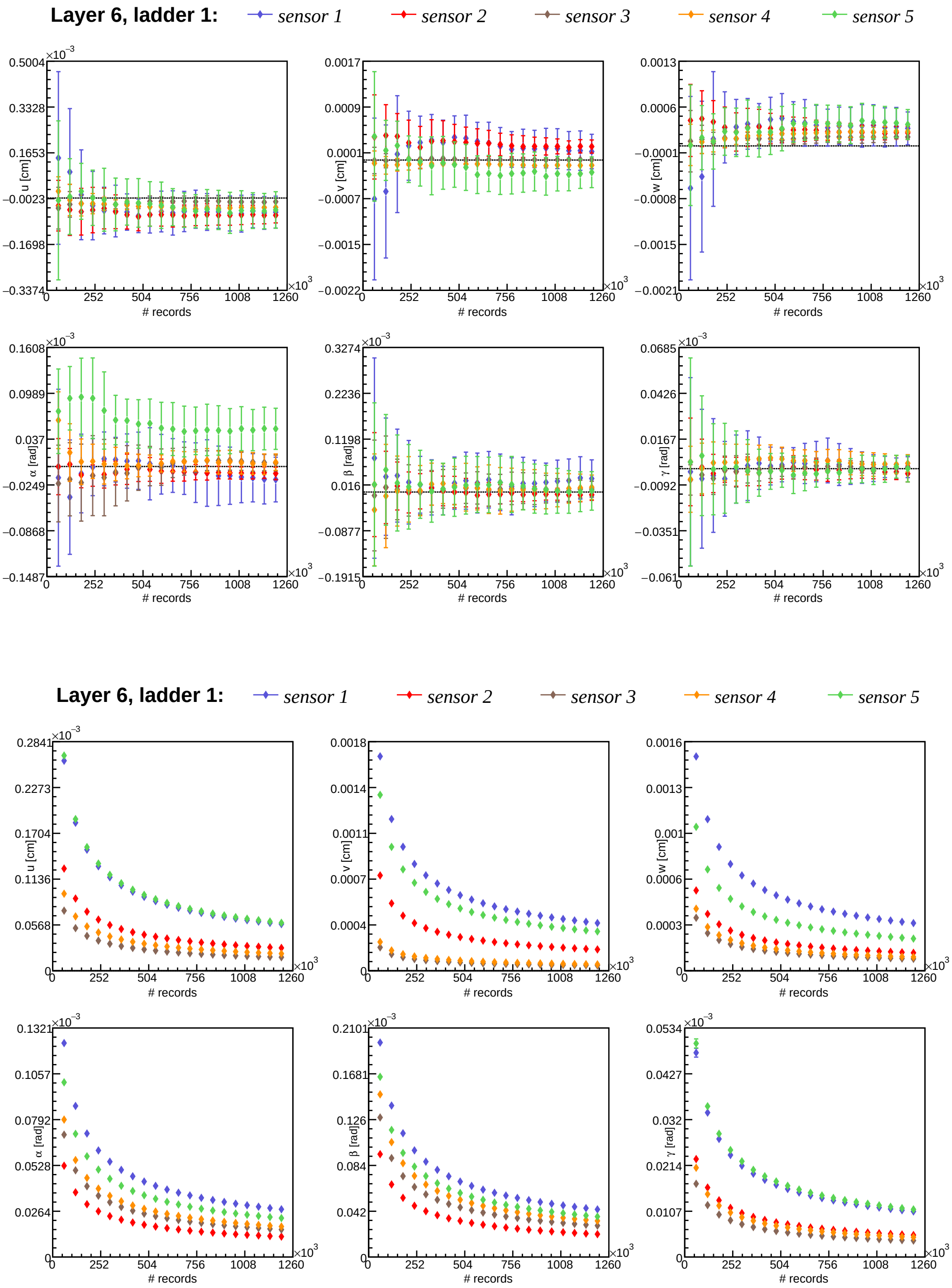

Figure 3.10: *The convergence study of the muon pairs dataset for mean and standard deviation calculated by the Millepede algorithm:* The top half shows means for each alignment parameter. The dotted line shows ideal alignment. The standard deviations of alignment parameters are shown in bottom half. As can be seen (most clearly in the plots on the left), the algorithm converges quite fast, but not necessarily to the correct (zero) values.

3.5 Weak modes

The matrix $\mathbf{C}'$ in equation 2.7 must be inverted to solve the system of equations for alignment parameters. However it may happen that this matrix is singular or ill-conditioned. Vanishing eigenvalues of the matrix correspond to weakly defined degrees of freedom, that is, to combinations of alignment parameters that cannot be estimated from the given dataset, since they leave the overall χ^2 unaffected. If the degrees of freedom of the alignment algorithm are not controlled enough, the singularity can affect the results of alignment procedure. This defects of alignment are called weak modes and typically can be seen as distinctive patterns of deviations. The weak modes can be seen in the cosmic ray dataset or the $\Upsilon(4S)$ dataset. For cosmic muons we can see weak modes in u and w coordinates. This weak mode is called ”twist”.

3.6 Mixing study

The mixing study aims at answering the following question: What mixtue of $\Upsilon(4S)$, cosmic ray and muon pairs data best eliminates weak modes and minimizes ranges of biases of the rotations and translations? We start with mixing two datasets. All combinations are shown in Fig. 3.11, Fig. 3.12 and Fig. 3.13, the ratio between datasets is 1:1. The results are calculated using the data of the convergence study.

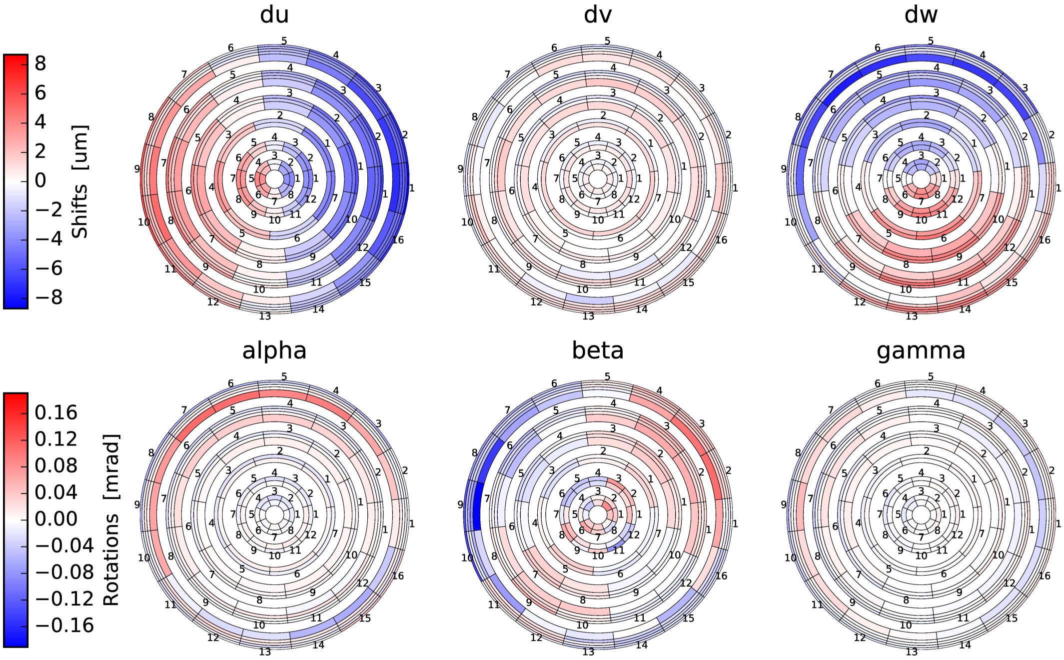

Figure 3.11: *Sixplots of biases for a 1:1 mixture of the* $\Upsilon(4S)$ *and cosmic datasets:* All patterns and ranges in the top line are inherited from the cosmic dataset. The ranges for rotations are smaller than for the cosmic dataset. This mixture fixes rotations better than any of the two datasets alone.

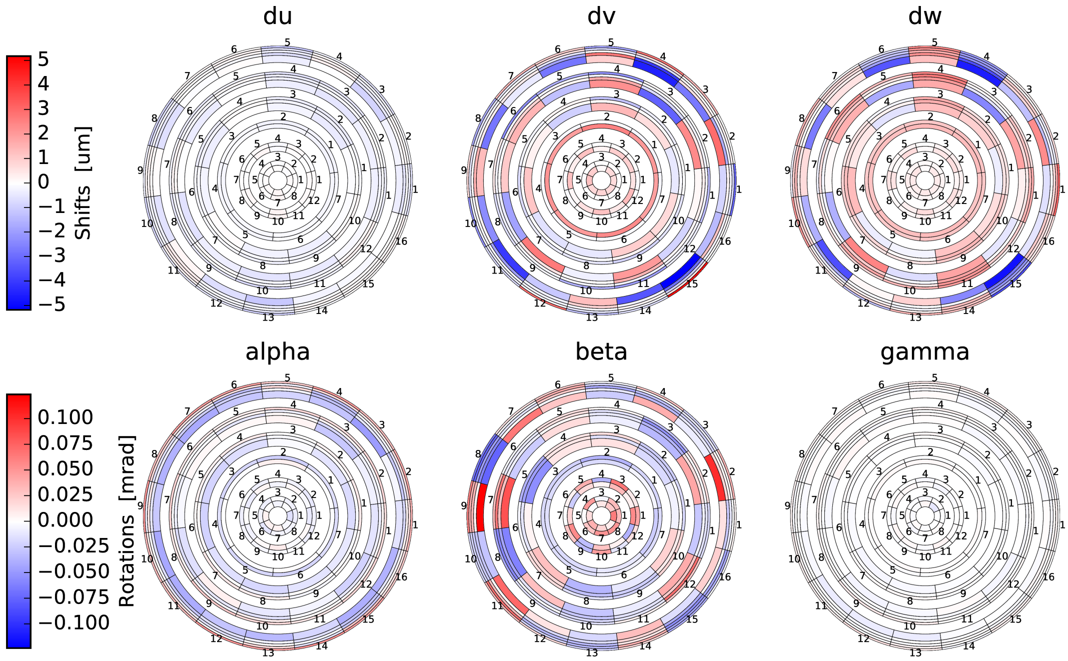

Figure 3.12: *Sixplots of biases for a 1:1 mixture of the* $\Upsilon(4S)$ *and muon pairs datasets:* All patterns and ranges are inherited from the muon pairs dataset. The $\Upsilon(4S)$ dataset does not fix enough alignment parameters.

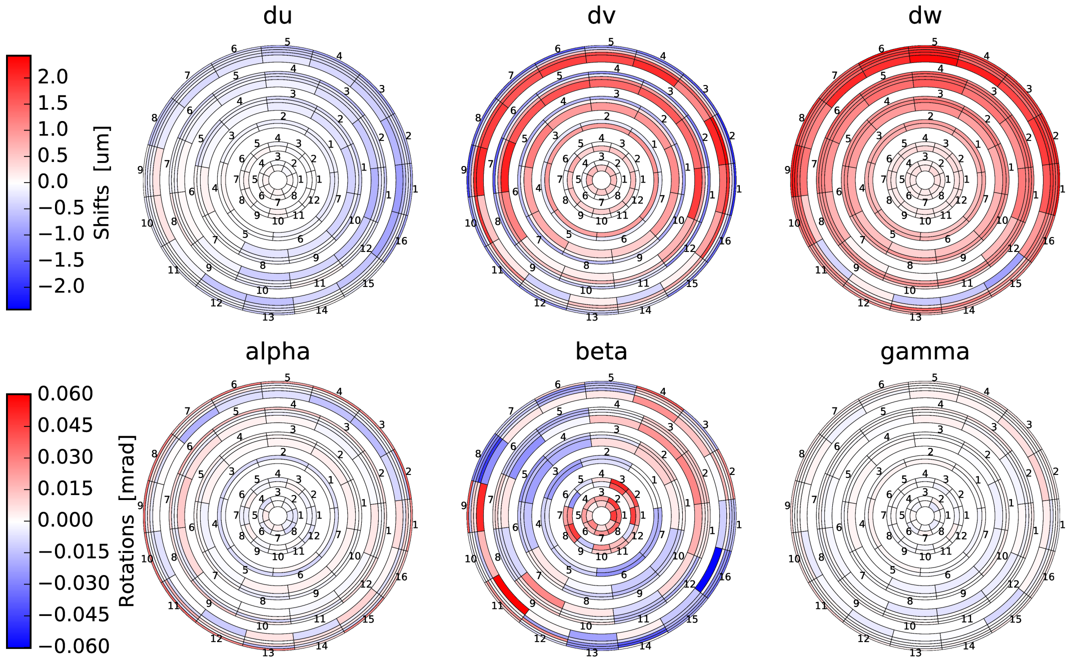

Figure 3.13: *Sixplots of biases for mixture of a 1:1 the cosmic and muon pairs datasets:* This mixture perfectly fixes all sensors shifts and rotations. The typical patterns in u, w shifts are no longer seen in the plots. The precise result in u and all rotation parameters are inherited from the muon pair dataset. This mixture fixes all sensors in v and w and produces a new type of pattern, which has not been seen before. The ranges for rotation and translation parameters are the best we have ever got.

According to Fig. 3.13 we have successfully eliminated much of the observed weak modes. There are the smallest ranges for rotation and translation parameters. However, combination of all datasets can eliminate even these atypical patterns. If we want to map the mixing ratios of the 3 datasets with 0.05 step, we have to calculate 231 alignments. The quality of each alignment is measured by residual χ^2 defined as sum of parameter biases divided by their estimated errors. The resulting χ^2 values are shown in Fig. 3.14. The ”optimal mixture” is 11 $\Upsilon(4S)$ to 2 cosmic and to 7 muon pair. The comparison between the mixture of the cosmic and muon pair datasets and optimal mixture is in Fig. 3.14. The mixture with the smallest χ^2 value of residual misalignment is shown at Fig. 3.15.

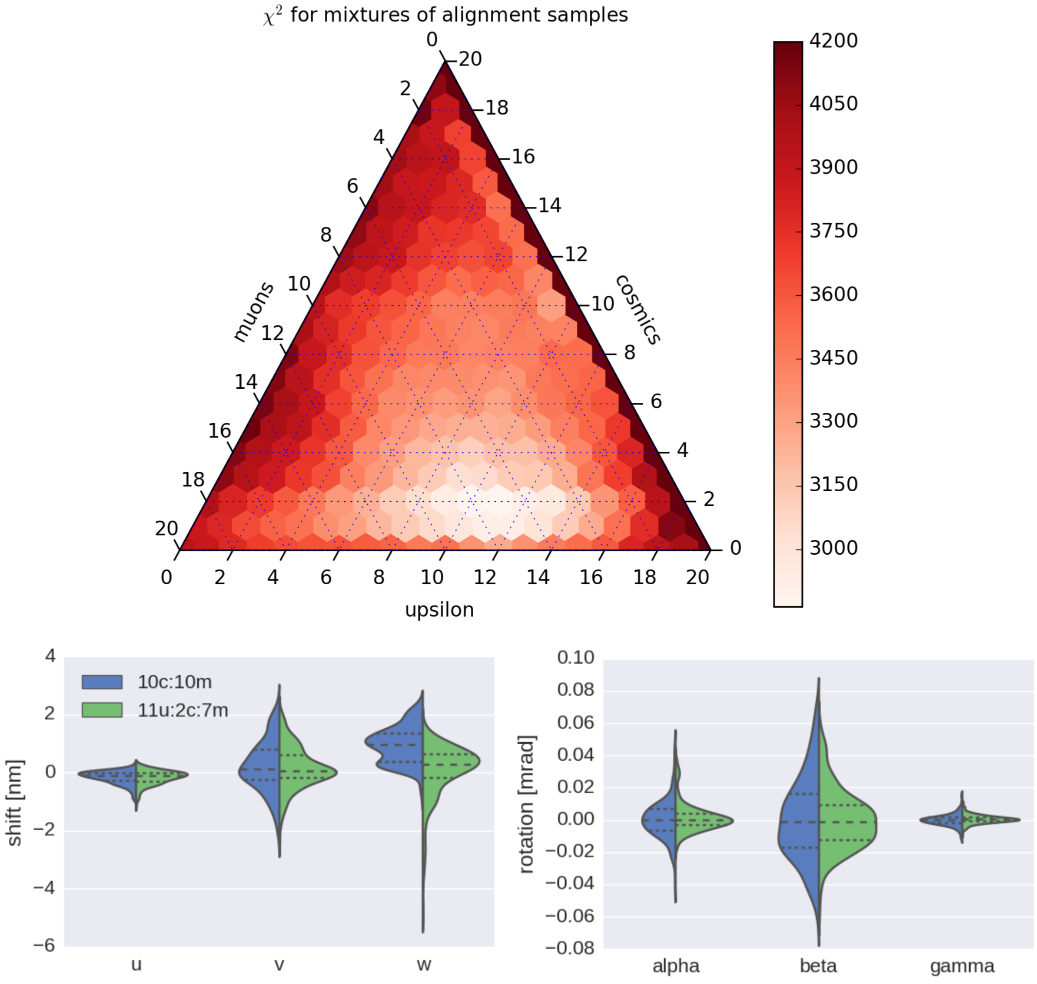

Figure 3.14: *Mixing Triangle:* The ternary plot (top) shows χ^2 for all mixtures of the three datasets. The vertices of the triangle show ”clean” datasets, the sides represent mixture of two datasets. The best choice is the mixture with ratio 11u:2c:7m. *Comparison of mixtures:* The bottom violin plots show the distribution of shifts (left) and rotations (right) for two mixtures: 10c:10m(no upsilon), and the optimum from the triangle diagram, 11u:2c:7m.

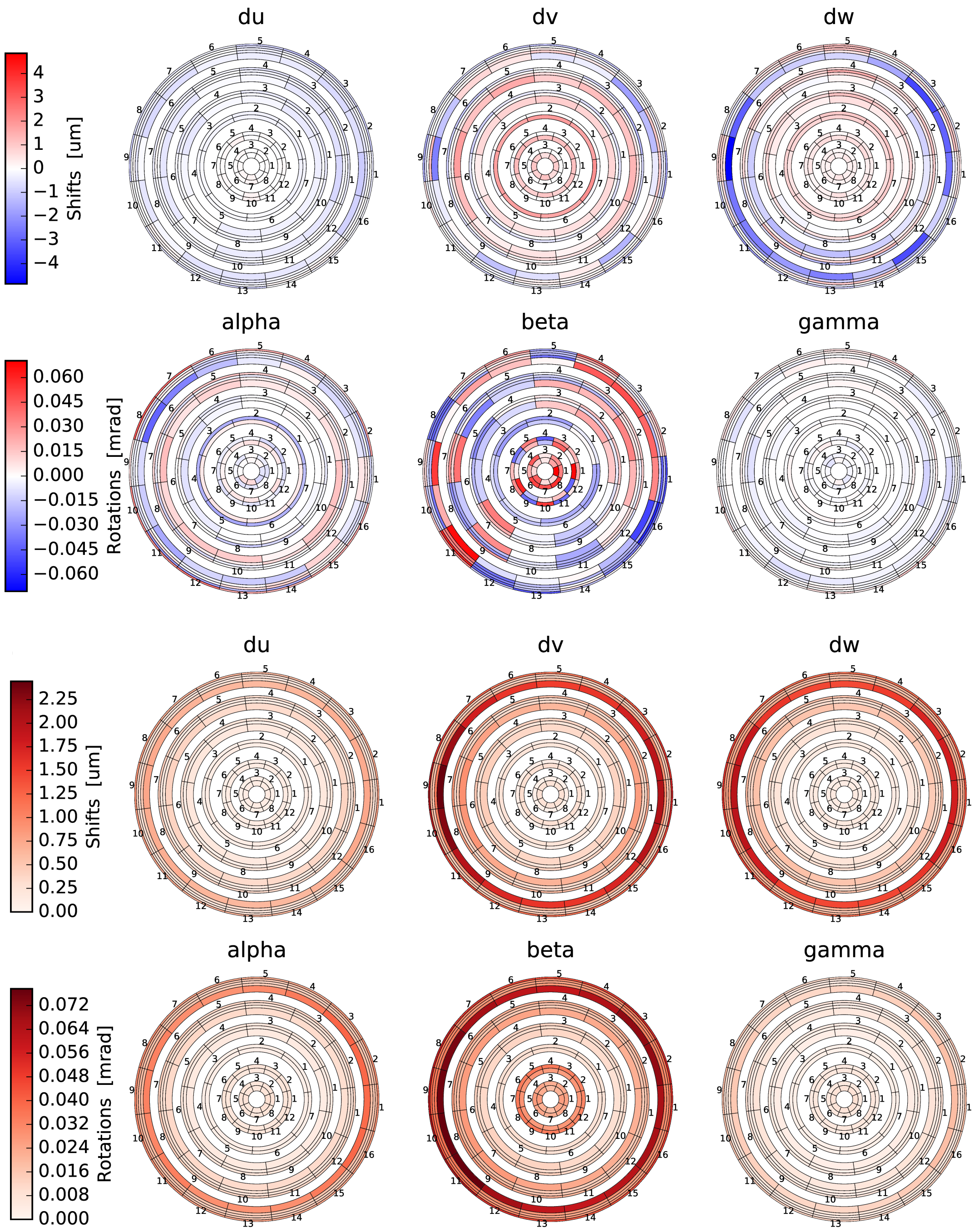

Figure 3.15: *The mixture of datasets with ratio 11u:2c:7m:* The six ring plots in top show bias. The six ring plots in the bottom represent standard deviation estimated by Millepede. The range of shifts is slightly worse than for the mixture of cosmic and muon pair dataset. The difference is due to poorly constrained fixed wedge sensors in the sixth layer. The same issue is shown in ring plots of deviation. The highest values of deviation are assigned to the wedge sensors. The rotations are similar to the rotations for the mixture of cosmic and muon pair datasets. Another source of error is the poor resolution in β angle. This angle corresponds to rotation of sensors around their long axis. Fixation of this rotation requires low p_t tracks, and therefore depends on successful reconstruction of curlers, which is a challenge for tracking.

4. Convergence of alignment

The study presented in this section follows a different scenario: We randomly misalign VXD sensors by applying random shifts and rotations to individual sensors. We generate tracks though the detector and apply alignment to recover the correct geometry. We study the degree of recovery as a function of severity and type of initial misalignment. Also, in this section we use real clustering for simulated hits. (that is, not Monte Carlo true hits as in previous section).

To compare misalignment and computed alignment parameters in residual misalignment, we fix the position of a single sensor, instead of using constraints. The reason is, that with constraints, the computed alignment is expressed in a different coordinate system - defined by the constraints. In such case, the computed misalignment needs to be first transformed to this coordinate system before it can be compared to computed. Because the software infrastructure does not support such comparisons, we used a simpler approach, where the vertex detector is aligned with respect to the position of a fixed sensor. With this approach, we can directly compare the generated misalignment parameter values with the computed ones. The fixed sensor is the first sensor in the first ladder in layer 1 (1.1.1).

A selection of misalignment situations is presented in the following figures:

- Shifts only: 3 μm and 50 μm standard deviation (in Fig. 4.1 and 4.2)
- Rotation only: 0.06 mrad and 1 mrad standard deviation (in Fig. 4.3 and 4.4)
- Shift and rotation 50 μm and 1 mrad in standard deviation (in Fig. 4.5)

The ranges of generated misalignment parameters and calculated values of residual misalignment are shown in Table 4.1. Values of standard deviation residuals are compared with results of alignment study on nominal geometry (in first numeric column). The alignment procedure converges to virtually the same final alignment even with very large misalignments.

	Figure		4.1	4.2	4.3	4.4	4.5
Initial	Shifts [μm]	0.00	10.2	157.7	0.0	0.0	215.7
	Rotations [$mrad$]	0.000	0.000	0.000	0.247	3.040	3.467
Residual	Shifts [μm]	4.62	4.11	4.06	4.15	4.09	4.35
	Rotations [$mrad$]	0.086	0.106	0.106	0.104	0.104	0.104

Table 4.1: Convergence of alignment

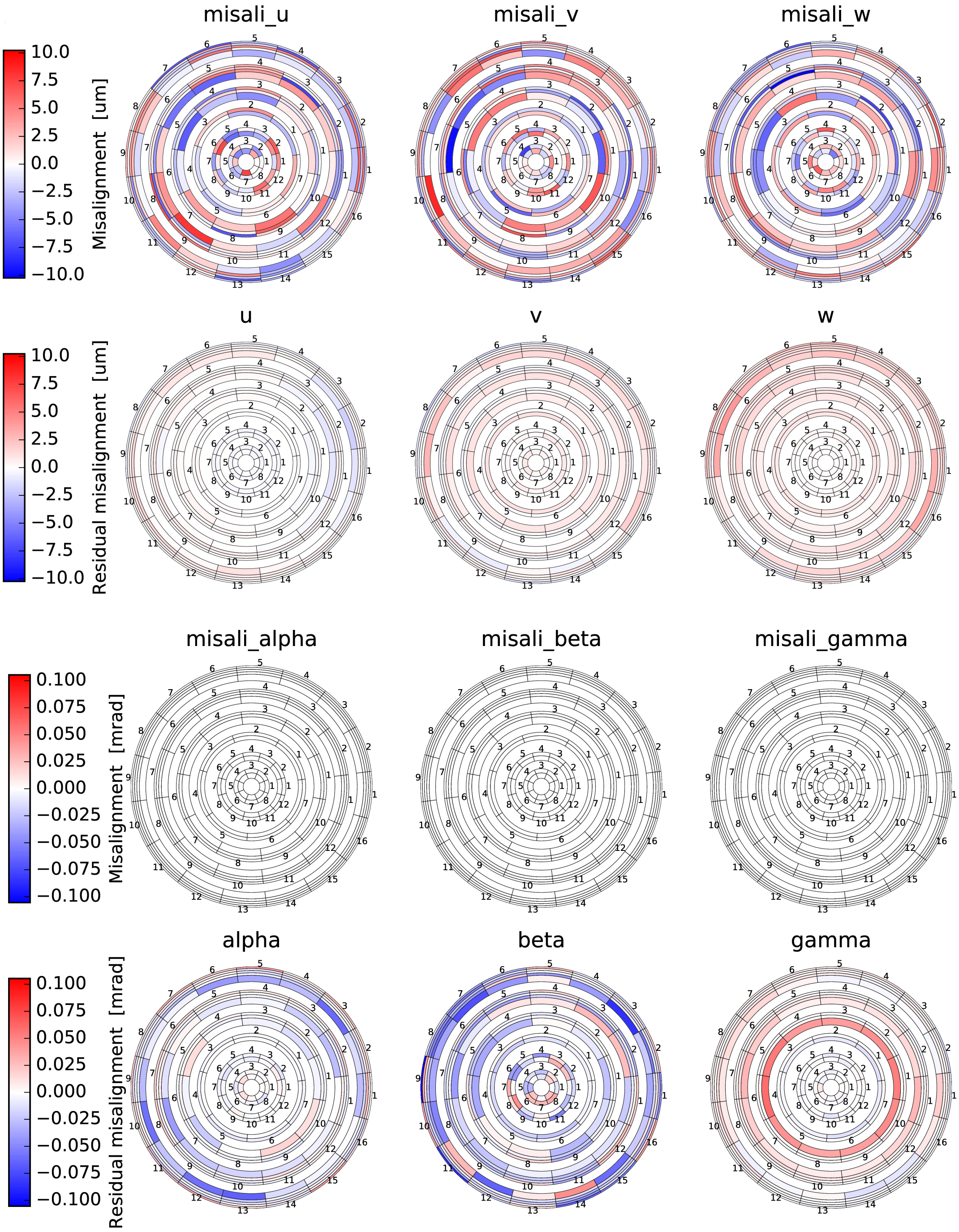

Figure 4.1: *Re-alignment of a geometry with shifts randomly misaligned with standard deviation 3* μm*:* The first and the third rows of plots show the shifts and rotations of misaligned geometry, the second and the fourth rows show the re-aligned shifts and rotations, respectively. Apparently, the re-aligned leads to a residual pattern similar to those we are seen in the previous chapter.

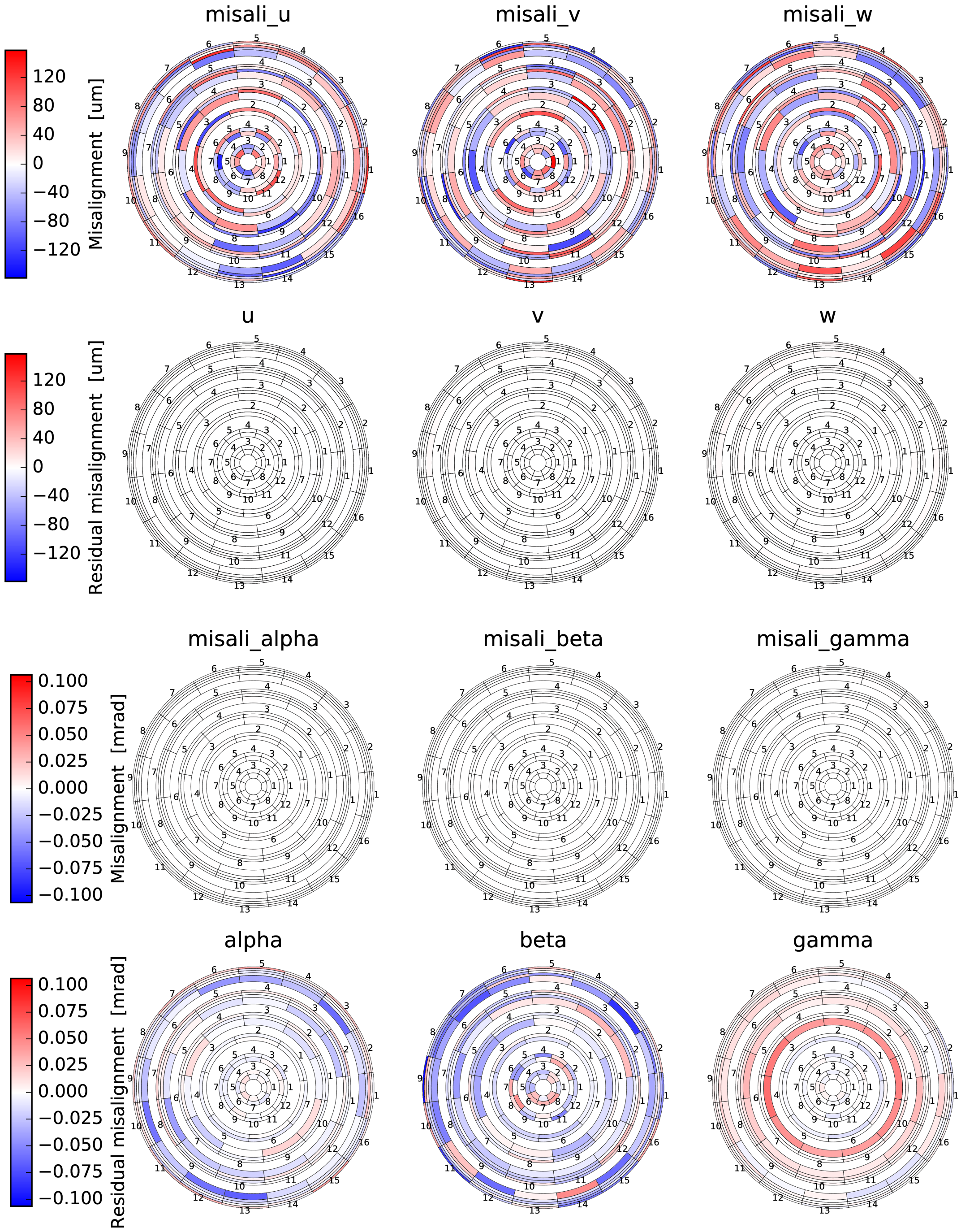

Figure 4.2: *Re-alignment of a geometry with shifts randomly misaligned with standard deviation 50* μm*:* The first and the third rows of plots show the shifts and rotations of misaligned geometry, the second and the fourth rows show the re-aligned shifts and rotations, respectively. Apparently, the re-aligned leads to a residual pattern similar to those we are seen in the previous chapter. The range for shifts is 10 times higher than in Fig.4.1

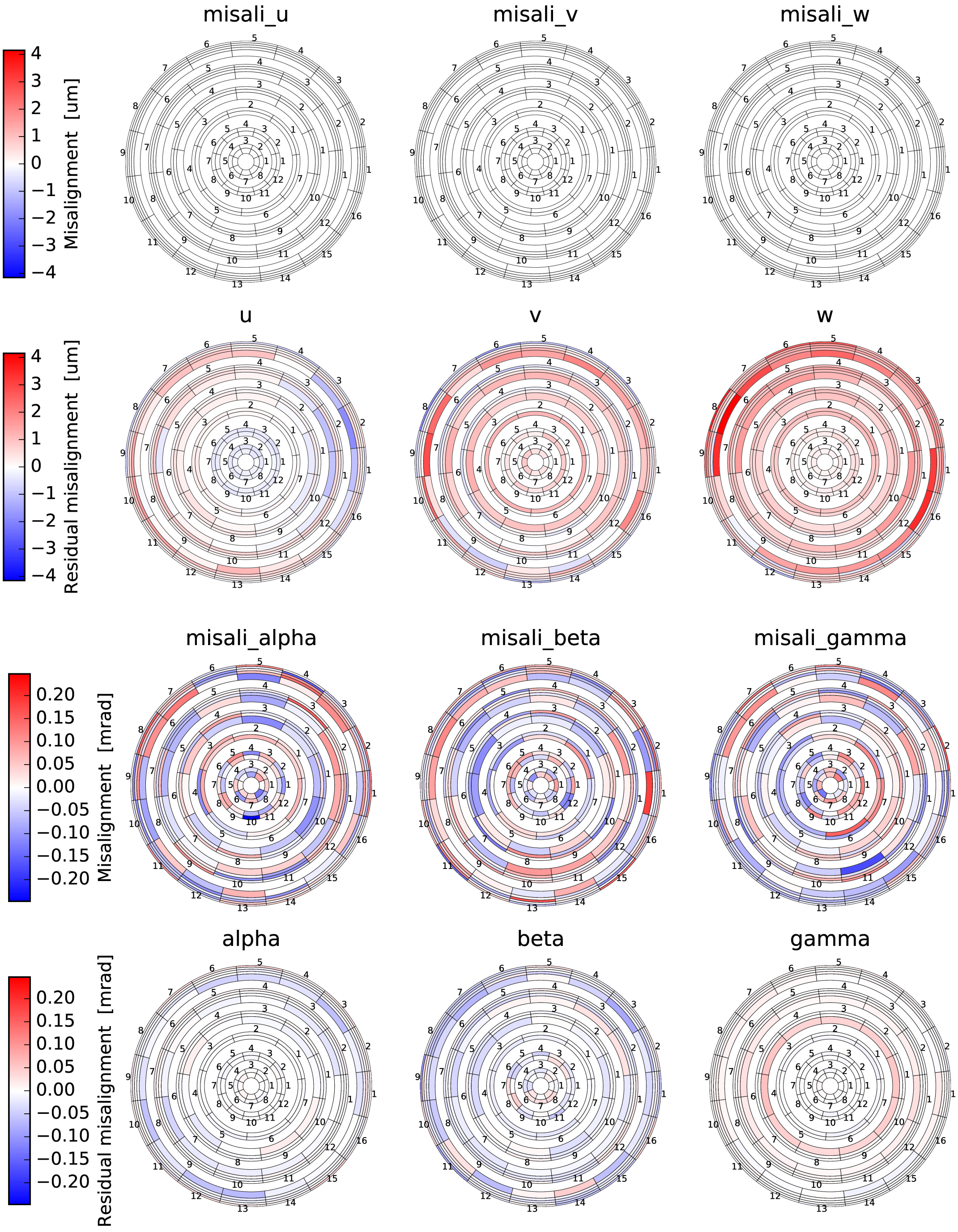

Figure 4.3: *Re-alignment of a geometry with rotations randomly misaligned with standard deviation 0.06 mrad:* The first and the third rows of plots show the shifts and rotations of misaligned geometry, the second and the fourth rows show the re-aligned shifts and rotations, respectively. Apparently, the re-aligned leads to a residual pattern similar to those we are seen in the previous chapter.

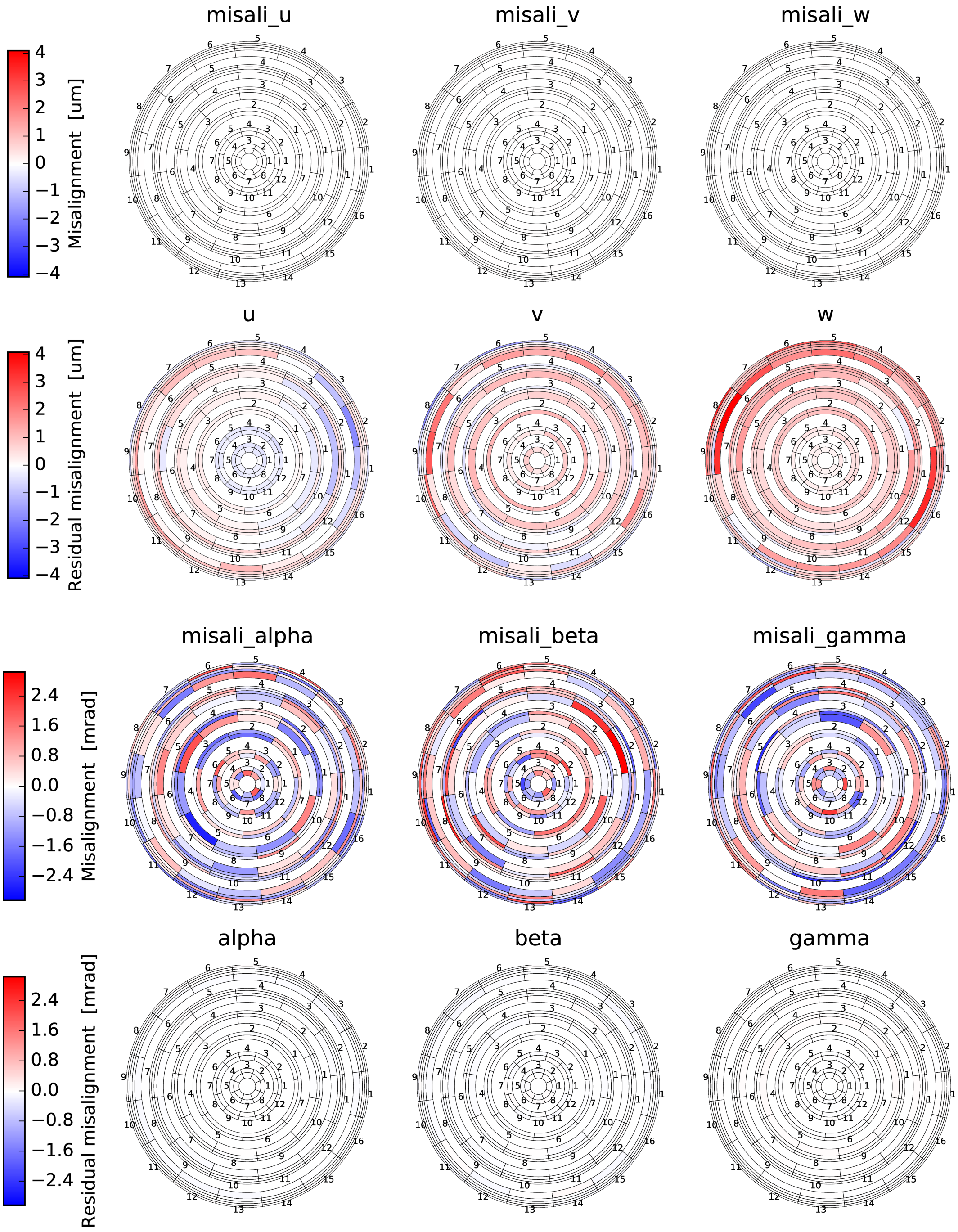

Figure 4.4: *Re-alignment of a geometry with rotations randomly misaligned with standard deviation 1 mrad:* The first and the third rows of plots show the shifts and rotations of misaligned geometry, the second and the fourth rows show the re-aligned shifts and rotations, respectively. Apparently, the re-aligned leads to a residual pattern similar to those we are seen in the previous chapter. The range of rotation is 10 times higher than in Fig.4.3

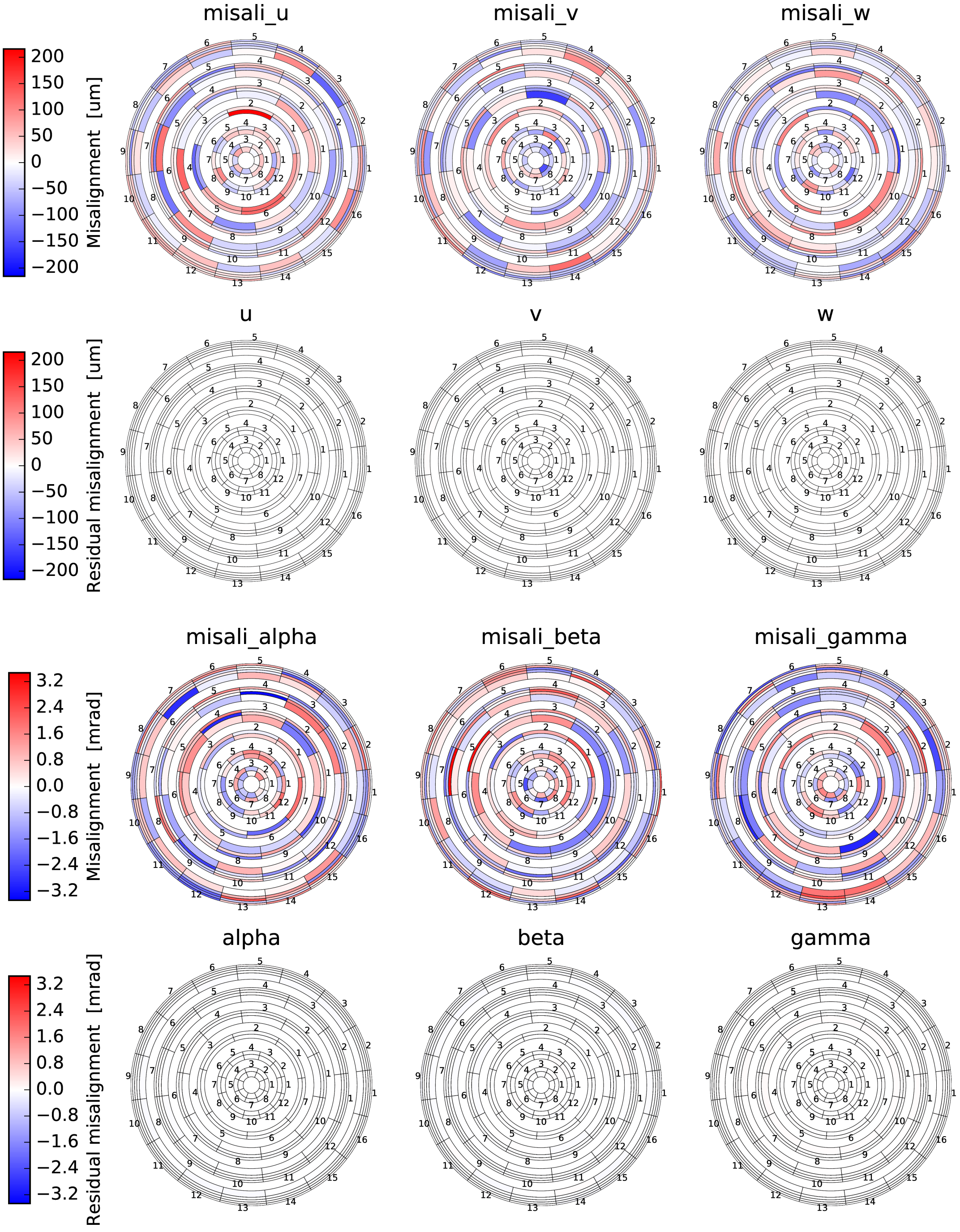

Figure 4.5: *Re-alignment of a geometry with randomly misaligned shift with standard deviation 50* µm *and rotations with standard deviation 1 mrad:* The first and the third rows of plots show the shifts and rotations of misaligned geometry, the second and the fourth rows show the re-aligned shifts and rotations, respectively. Apparently, the re-aligned leads to a residual pattern similar to those we are seen in the previous chapter.

5. Effect of misalignment on physical analysis

The question we address in this section is: What is the impact of the misalignment on physical analysis? What is the critical size of misalignment over which misalignment significantly affects the result of physical analysis. For the analysis we use the "golden channel" of B factories, $B^0 \to J/\Psi + K_{short}$.

We generate the misalignment by randomly shifting and rotating each VXD sensor by an amount taken form a zero-mean normal distribution. The standard deviation of the generated normal distribution is a measure of size of the misalignment.

For the study, we selected a set of physical observables:

1. ΔT, the time difference between the decays of B-mesons
2. Vertex positions of the B-mesons and other particles

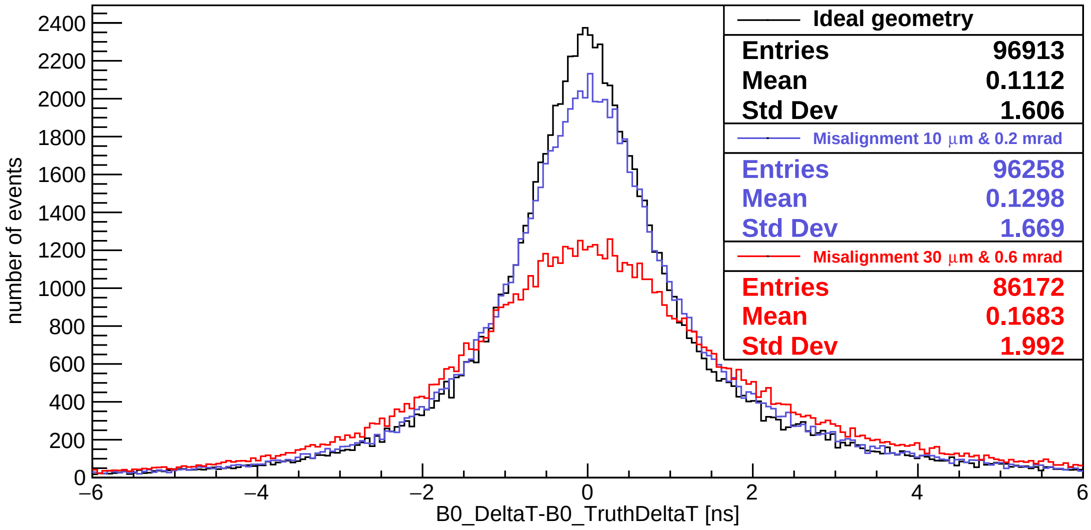

Figure 5.1: *Effects of misalignment on the distribution of* ΔT*:* The plot shows the distribution of ΔT for three misaligned geometries.

The effect of misalignment on the distribution of ΔT is shown in Fig. 5.1. The effect of misalignment as a function of misalignment size is shown in Fig. 5.2.

Apparently, the width of ΔT is only moderately affected by misalignment. The right plot of Fig. 5.2 offers a clue: the adverse effect of misalignment on the quality is masked by reconstruction filters on the quality of reconstructed tracks and vertices, and with increasing misalignment the rate of successfully reconstructed events decreases.

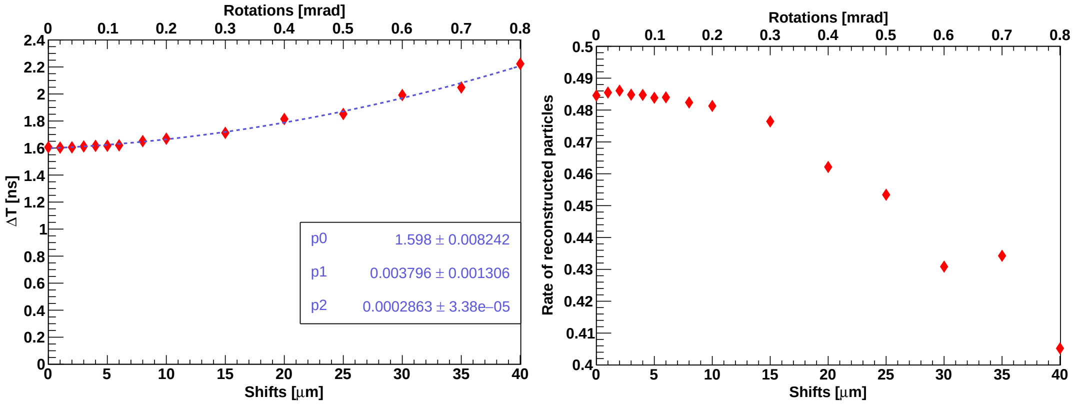

Figure 5.2: The width of ΔT distribution (left) and the rate of reconstructed particles (right) as a function of misalignment size.

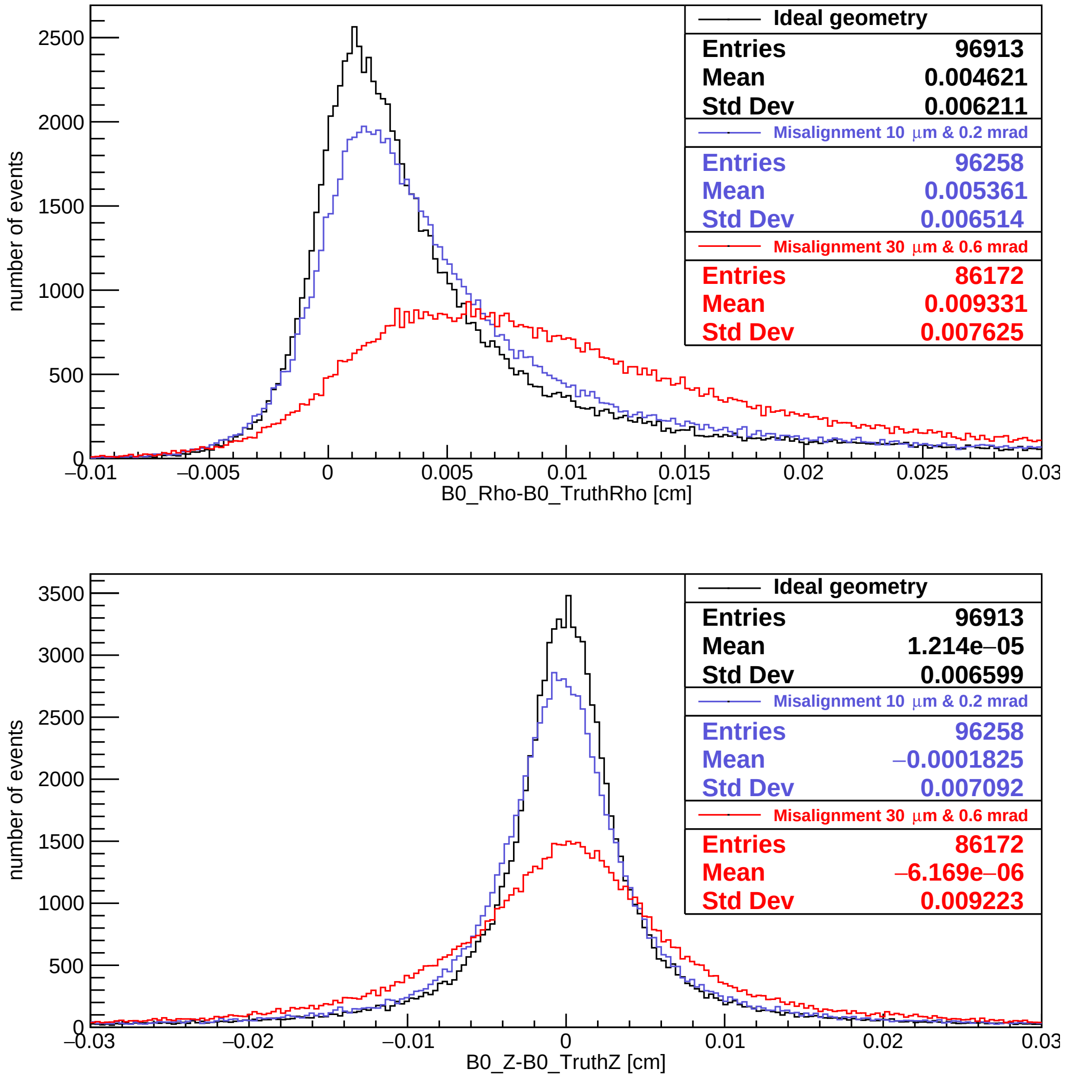

Figure 5.3: *Effects of misalignment on the distribution of vertex position of* B^0*:* The plots show the distribution of vertex position ρ (top) and z (bottom) for three misalignment geometries.

The plots in Fig. 5.3 show a different quantity, the difference between reconstructed and MC-true coordinates of B^0 vertices at various misalignment.

We can use a χ^2 measure to measure the effect of misalignment on distribution of a physical parameter. This allow us to estimate the size of critical misalignment, over which the effects of misalignment become critical. This is illustrated in Fig. 5.4. The idea is that for small misalignment, we cannot discriminate between the effect of misalignment and statistical variability of the unperturbed distribution. We therefore define the χ^2 of critical misalignment as the critical value of the χ^2 test on the difference between a given and the unperturbed distribution. This also gives a logical link between the amount of data available and a minimal detected misalignment.

The green bands in plots of Fig. 5.4 are areas where misalignment cannot be detected on the background of statistical fluctuation of nominal alignment distribution. Apparently, the critical misalignment has standard deviation 3.0 μm in shift and 0.06 mrad in rotations. This is very close to parameters of residual misalignment we achieved in previous sections. We can therefore conclude that our alignment procedure, as crude as it currently is, can suppress even large misalignment to a degree that makes the result of physical analysis virtually unperturbed.

The MC-based quantities used in this section are not usable for monitoring during a physics run. In the following section, we introduce processes and quantities intended just for this purposes.

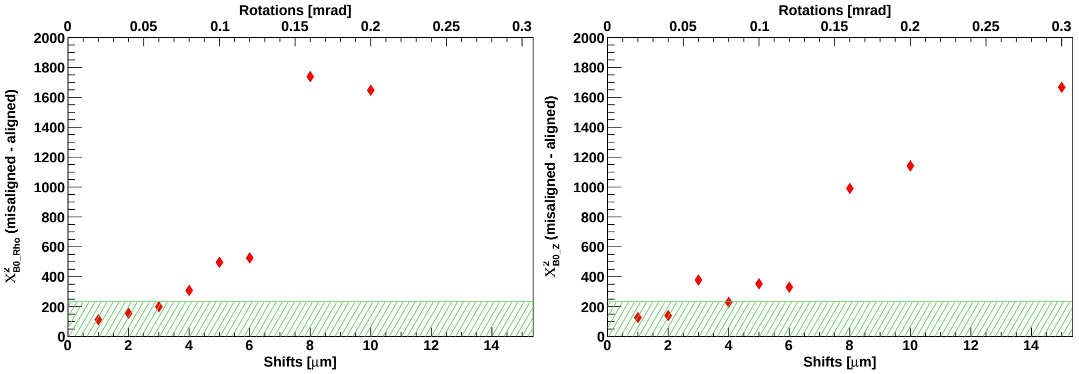

Figure 5.4: χ^2 *distance from nominal distribution as a function of misalignment size:* Values of χ^2 for ρ position (left) and Z position (right) of B^0 vertex. The green region shows an acceptance box for misalignment based on the χ^2 distance of distributions. In other words, misalignments with χ^2 within the green box give distribution indistinguishable from the nominal distribution.

6. Alignment validation and monitoring

The MC-based quantities used in the previous section are not usable for monitoring of (mis-) alignment. We need processes and quantities that are observable in reconstruction, and which can be simulated so that the whole alignment procedure including (mis-) alignment monitoring can be validated using simulations. Despite of alignment algorithm converging, the predicted positions of modules do not correspond to the real ones. All kinds of misalignments which alter the reconstruction of the underlying physics need to be eliminated. Our alignment validation procedure under development is based on the analysis of cosmic-ray tracks and a decay with a high counting rate. This material is based on my final report from a DESY Summer Student Programme 2015 [38].

6.1 Validation and monitoring using a process with high counting rate

For validation and monitoring of alignment, one can select events from a well-studied physics process with a high counting rate and physics distributions that can be used as references. One of such processes is a decay of D^{*+} to D^0 and a positively charged pion π_{slow} with very small momentum (see Fig. 6.1). This process is selected from decay chain [39] [40]:

$$e^-e^+ \to c\bar{c} \to \mathrm{XD}^{*+} \tag{6.1}$$

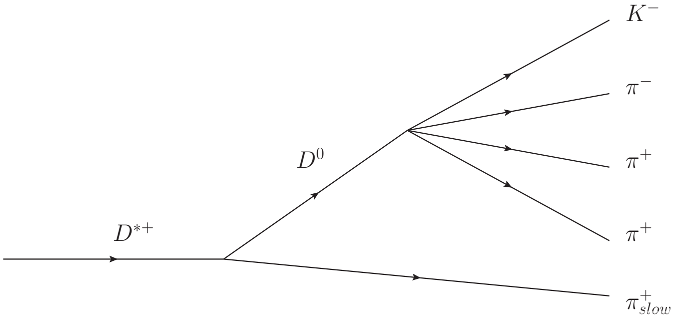

Figure 6.1: A decay chain $\mathrm{D}^{*+} \to \pi^+_{slow}\mathrm{D}^0(\to \mathrm{K}3\pi)$.

The neutral D^0 estimation from single space point to four particles. It can be used for vertex resolution and comparison of Monte Carlo prediction to real data result. The produced particles are two positively charged π^+, negatively charged π^- and a K^-, this decay of D^0 is referred to "K3π" in the following. A vertex candidate can be constructed by intersecting two tracks. The obtained vertices must coincide. The distance between the vertices, projected to each of the three coordinates, is interpreted as resolution effect.

In the analysis, only one produced D^{*+} per event is used. In the detectors we observe five charged particles. From tracking detectors, momenta and positions of particles in the final state are reconstructed. For the reconstruction of D^0, we use pairs of particles and reconstruct their vertices from particles with the same charge $((+\times+)\times(-\times-))$ and particles with different charges $((+\times-)\times(+\times-))$. In Fig. 6.2 residuals defined as differences between each component of the vertex positions are presented. These residuals will be used as reference plots.

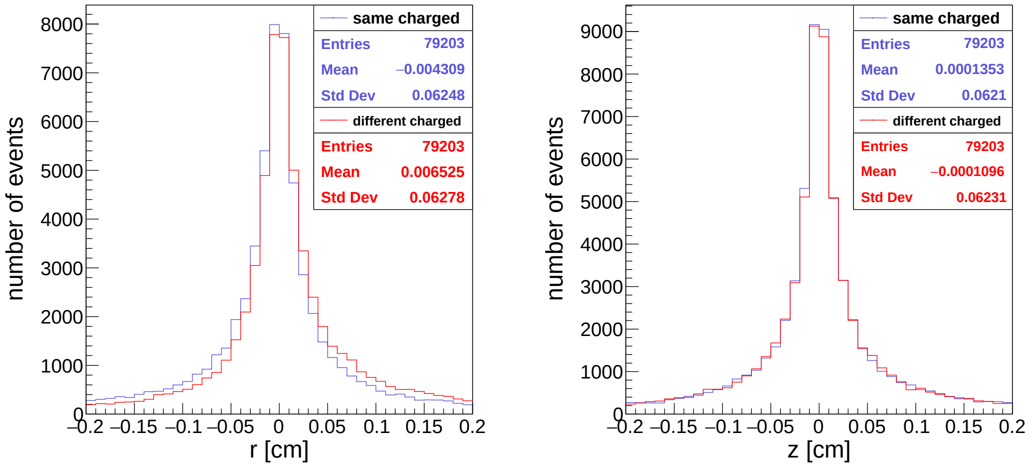

Figure 6.2: *Residuals as reference plots:* Residuals of reconstructed vertices in r-component of cylindrical system (left panel) and in z-component (right panel) for particles with the same charge (blue) and the particles with different charge (red).

From kinematic parameters of the reconstructed particles one can calculate invariant masses of D^0, D^{*+} and the sum of momenta of produced particles. The invariant masses are fitted using three different functions (Gaussian, Breit-Wigner, and Crystal ball as a signal and Chebyshev function of the second order as a background, where is necessary). The result of fitting with the smallest χ^2 are used in the analysis and shown in the figures (Fig. 6.4 and Fig. 6.5).

From the kinematic parameters of all reconstructed particles, including the pion with low momentum, the invariant mass of D^{*+} is reconstructed (Fig. 6.4). The reconstructed invariant mass of D^{*+} and sum of momenta produced particles from D^0 are used in following conditions:

1. Sum of momenta of produced particles from the D^0 decay is required to be in the interval between 2.5 and 6.0 GeV.
2. Invariant mass of D^{*+} is required to be in the range of two standard deviations from the mean value of the fitted function.

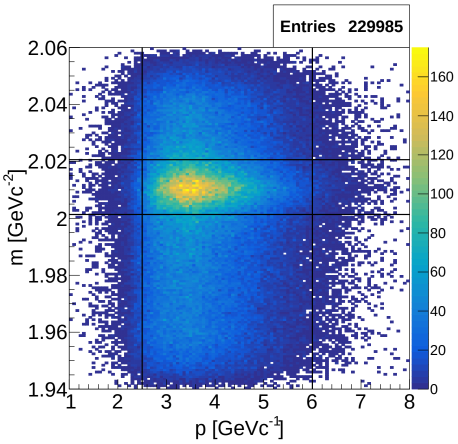

Figure 6.3: *Conditions for signal selection:* Here is shown mass of D^{*+} as a function of the sum of momenta of produced particles from D^0 decay. Straight lines present kinematic conditions used for selection of background.

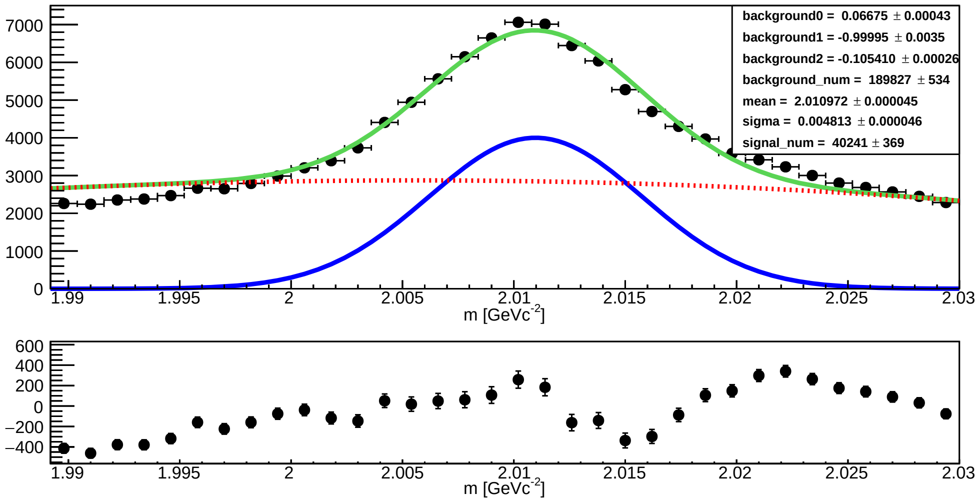

Figure 6.4: Invariant mass of D^{*+} (top panel): data (black points), a fitted signal (Gaussian blue curve), a background (dotted red curve) and the sum of the signal and the background (green). Residuals of the fit (bottom panel).

These conditions for better selection of the signal decay and rejection of the background are shown in Fig. 6.3. The events, which satisfy the conditions, are used in validation procedure and for reconstruction of invariant mass of D^0. The results of the kinematic analysis are shown in Fig. 6.5 and it will be used as a reference plot for alignment validation and monitoring.

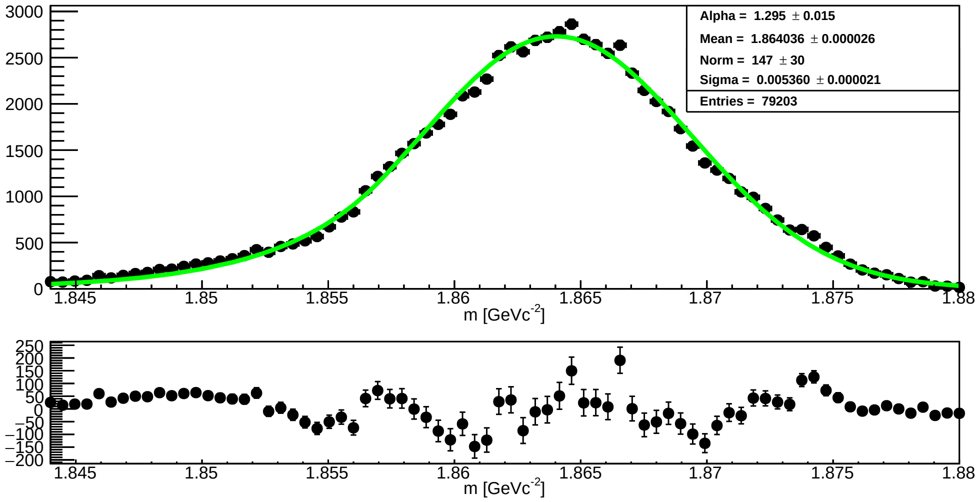

Figure 6.5: Invariant mass of D^0 after the selection (top panel): fitted data (black points) and the signal (Crystal ball green curve). Residuals of the fit (bottom panel).

6.2 Alignment validation and monitoring using cosmic rays

One can use cosmic particles (mainly muons) for alignment and calibration of tracking detectors, because muons pass through all the tracking detectors at different angles and can be detected in the Belle II tracking system. In the magnetic field, cosmic muon trajectories can be approximated by helices, therefore, track finding methods can be easily tested.

For validation and monitoring, we generate particles by CRY generator with specific settings: geographical information of the Belle II experiment, the volume of the keep and accept boxes the same as a cube with the side of 7.0 m. The global box is set as a cube with the side of 300.0 m and the generation plane is defined with the side of 300.0 m. We perform the simulation using all secondary particles and their minimum kinetic energy set to 10 MeV. The date is set to 6. June 2017 when cosmic tests of the Belle II detectors are planned.

A comparison between the number of generated and reconstructed particles is presented in Fig. 6.6. The momentum distribution of generated and reconstructed muons is also shown in the figure. Mainly muons are detected in the Belle II tracking system because other particles cannot pass through the Belle II outer detectors.

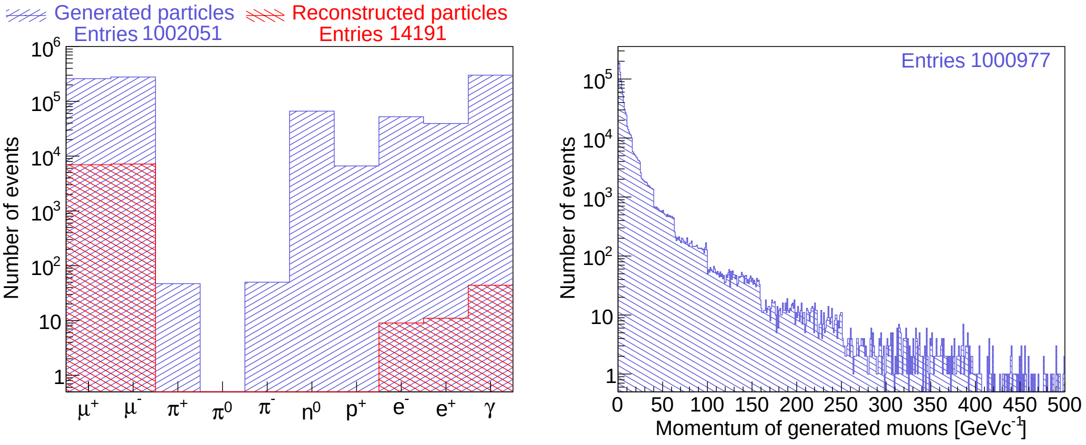

Figure 6.6: Number of generated (blue) and reconstructed (red) tracks (left panel) and momentum of generated (blue) muons (right panel).

For the cosmic track reconstruction, the Trasan track finder developed for the Belle experiment and implemented in basf2 was used. This track finder was optimized for the search of tracks mainly coming from the interaction region assuming particles propagating from inside the detector to the outside direction. Therefore, for a cosmic track, Trasan finds two tracks (in CDC): one in the top part of the detector and the other in the bottom part. If a cosmic particle passes the CDC, in most of the cases only one cosmic muon is present and two tracks are found by Trasan. Using the knowledge that these two found tracks are the two parts of the same cosmic muon, one can compare the reconstructed track parameters of two track parts. In case of ideal alignment, the reconstructed track parameters of two track parts should coincide within the track reconstruction uncertainties. Also, because these two track parts are reconstructed independently, there should be no correlations between different track parameter residuals.

In these studies we define reference plots in order to show the differences between kinematic parameters of these two parts of the track. The reference plot is a matrix, which has the distribution of differences of the track parameters in the diagonal part and the correlations between the track parameters in the non-diagonal part. A color of background in the non diagonal part of the matrix corresponds to the values of correlations (green for $corr \sim 0$ and red for $corr \sim \pm 1$). The correlations are defined as:

$$corr = \frac{\sum_{i=1}^{N}(x_i - \bar{x})(y_i - \bar{y})}{\sqrt{\sum_{i=1}^{N}(x_i - \bar{x})^2}\sqrt{\sum_{i=1}^{N}(y_i - \bar{y})^2}}. \tag{6.2}$$

In case of misalignment, shifts in the residual distributions can be observed as well as larger correlations between track parameters. The reference plots for comics validation are shown in Fig. 6.7 for the Cartesian track parametrization.

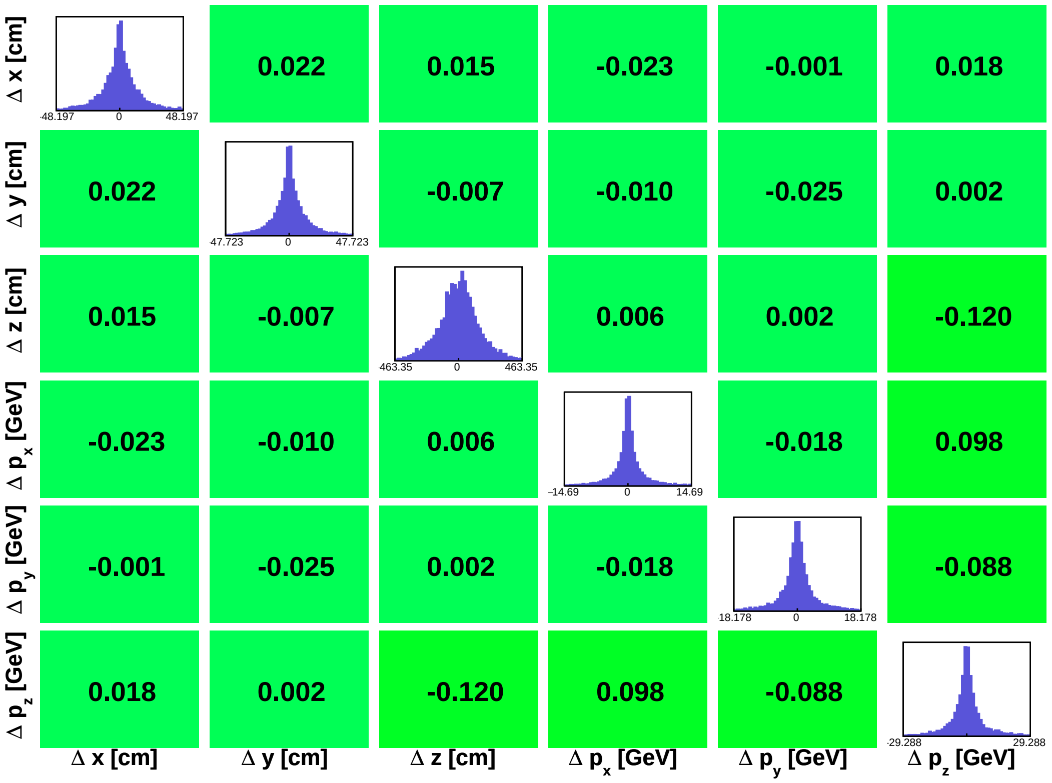

Figure 6.7: *Reference plot for Cartesian coordinates:* residuals (diagonal) and correlations (non-diagonal).

6.2.1 Counting rate of cosmic rays

At Belle II, the Belle Trasan is being replaced by a more advanced CDC local track finder under development [41] based on a cellular automaton. This track finder is able to find full cosmic tracks without splitting them to two parts. Our study is focused on comparison between these different track finders, shielding of subdetectors at reconstruction of cosmic rays and looking for issues with application different magnetic field models.

The shielding effect of Belle II subdetectors is illustrated at Fig. 6.8. The CDC is necessary for the counting rate study, since it detects cosmic muons. Other outer detectors, which are not used for detection of charged tracks, are only a shielding material for cosmic muons. Geant4, the simulation engine of Belle II, uses a geometry that is comprised only from the subdetectors of Belle II. The building, where Belle II detector is located, is not included in the simulation framework. Because of that the simulated values for cosmic are not realistic. During data taking of cosmic muons our calculated numbers must be renormalized. We think that a realistic number should be smaller than that presented in this thesis. The study has been done for both track finders. The Trasan recognizes (57.5 ± 2.7) % of muons observed by the CDC local track finder. Using the KLM detector the counting rate decreases by about 20 % because of material budget of KLM. The KLM removes or captures cosmic muons with initial momenta up to 1.5 GeV (Fig. 6.8).

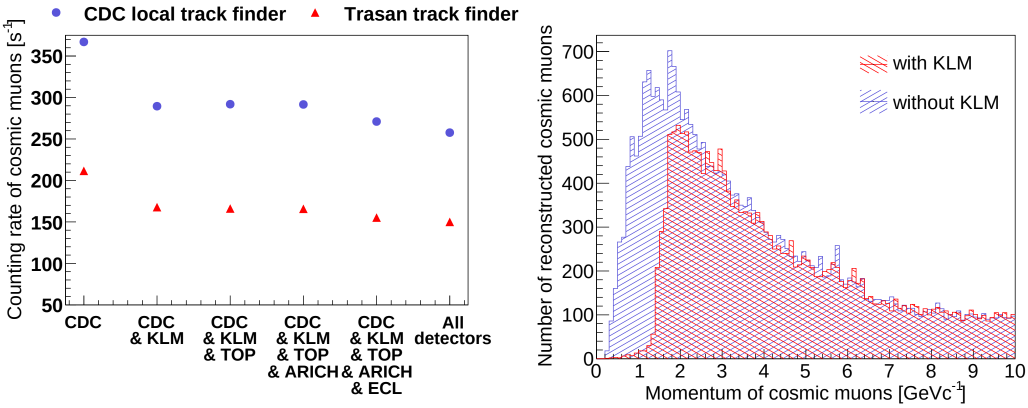

Figure 6.8: *Counting rate as a function of outer detectors:* The left figure shows counting rates for both track finders. The decreasing muon rate including KLM is explained in the right plot. The cosmic muons with momenta smaller than 1.5 GeV are caught by the top part of KLM.

A magnetic field is necessary for calculation of momenta of reconstructed charged tracks. The Belle II simulation framework provides three models of magnetic field:

- *MagneticField:* Constant magnetic field of 1.5 T in the volume enclosed by the magnet coil.
- *MagneticField2D:* Magnetic field calculated according to a realistic magnetic field map.

- *MagneticFieldRCDC:* Constant magnetic field of 1.5 up to outer border of the CDC.

The counting rate of cosmics using three magnetic field models is shown in Fig. 6.9. The hits in the CDC do not depend on the magnetic field. The CDC local track finder works with hits, so we can calculate the counting rate from this information even if we do not use a magnetic field. For the Trasan track finder we can not use this information, because it works with momenta. The detected hits without a magnetic field are used for calibration and alignment study of CDC. The MagneticField is not recommended for simulation of cosmic tracks. This magnetic field scatters cosmic muons with low momenta in the z coordinate (Fig. 6.9. This issue should be accepted in a future cosmic analysis. The MagneticFieldRCDC is very similar to the realistic magnetic field for cosmic muons studies.

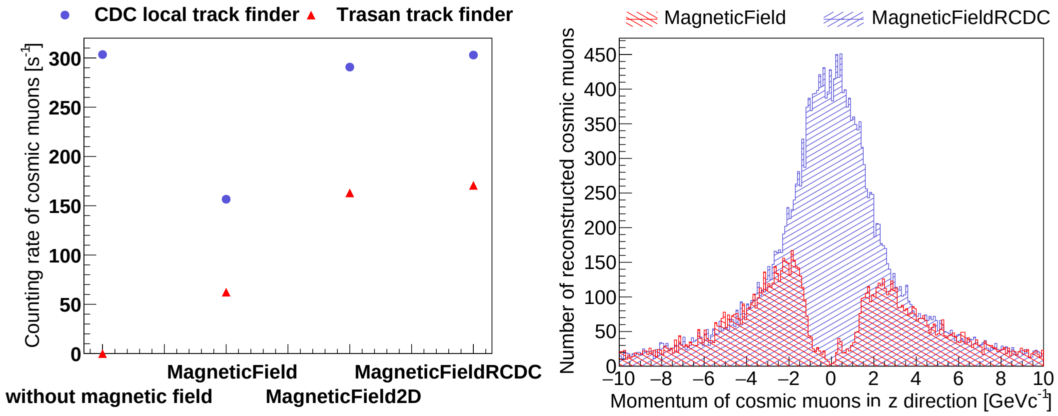

Figure 6.9: *Counting rate as a function of used magnetic field:* We show counting rate for individual magnetic fields used for reconstruction of charged particles in the CDC. For all magnetic fields the KLM is used only as a shielding detector.

Conclusion

In this thesis, I present the result of my studies of alignment of the Belle II VXD sensors - properties of residual misalignment, optimization of data samples for alignment, convergence properties, impact of misalignment on physical analysis and alignment validation and monitoring.

The review part starts with introduction to CP violation and its experimental studies. We then go on the Belle II experiment as a new generation B-factory, with a description of Belle II detector and software framework.

The central part of the review section is the introduction to alignment of silicon vertex detectors, the software tools used for alignment and calibration, with application to the Belle II vertex detector.

The experimental part starts with a section on the properties of residual misalignment and data sample optimization study. We show that the weak modes of VXD alignment can be strongly suppressed using an optimal mixture of $\Upsilon(4S)$, cosmic and muon-pairs samples. We also identified the degrees of freedom that need to be better fixed either by additional constraints or track samples: wedge sensors and rotation around the long axis of sensors. Fixing these alignment issues will later allow us to include additional degrees of freedom to alignment parameter space-such as deformations of sensors.

We have shown that the alignment converges to the same residual misalignment even for large initial misalignment.

The next studies show we study the effect of misalignment on physics observables. Using the χ^2 measure, we showed that misalignment under 3 μm standard deviation shifts and 0.06 mrad standard deviation rotations have insignificant (that is, indistinguishable from statistical variation) effect on physical analysis. These parameters are very close to the residual misalignment we are able to achieve with current alignment procedure for the Belle II VXD. We can therefore conclude that even the present alignment is good enough to suppress the effect of geometry misalignment on physical studies.

In the last section we present our result on the development of validation and monitoring of VXD alignment. Two different processes have been studied. The first process with a high counting rate $\mathrm{D}^{*+} \rightarrow \pi^{+}_{\mathrm{slow}}\ \mathrm{D}^0(\rightarrow \mathrm{K}3\pi)$. As a result of analysis, three reference plots are defined for this process (Fig. 6.2 and Fig. 6.5). The second method uses muons from cosmic rays. For this method, we show reference validation plots for Cartesian representations in Fig. 6.7.

The reference plots will be used in the future for monitoring of misalignment and miscalibration effects. It is necessary to do the same misalignment study for physical process $K3\pi$ as for "golden process" $\mathrm{B}^0 \rightarrow \mathrm{J}/\Psi + \mathrm{K}^0_{short}$ and check the sensitivity of chosen process for misalignment affects at the level of physical resolution. The validation procedure is not connected with silicon vertex detectors alone, but with central drift chamber too. It is necessary to do the same study using momenta and invariant mass using the validation channel.

The validation study concludes with the counting rate study. We have tested two different track finding methods. The CDC local track finder is more efficient, but it can not be used for validation using cosmic rays, because it is not able to split the cosmic track. Second, Trasan, is able to split track, but its counting rate is smaller. We show the shielding effects of subdetectors of Belle II (in Fig. 6.8) and issues of simulated magnetic fields in Belle II simulation framework (in Fig. 6.9). The counting rate from cosmic muons can be estimated for each tracking detector and compared with cosmic calibration measurements using the CRY cosmic-ray generator tested in these studies. These results will be helpful during preparations of simulation for cosmic run in future.

Bibliography

[1] *G. Isidori:* Flavor physics and CP violation, arXiv:1302.0661 [hep-ph]

[2] *J. H. Christenson, J. W. Cronin, V.L. Fitch, R. Turlay:* Phys. Rev. Lett. 13, 138 (1964)

[3] *M. Kobayashi, T. Maskawa:* Prog. Theor. Phys. 49 (1973) 652-657

[4] *K.A. Olive et al. (Particle Data Group):* Chin. Phys. C, 38, 090001 (2014)

[5] *J. J. Aubert et al.:* Phys. Rev. Lett. 33, 1404 (1974); *J. E. Augustin et al.:* Phys. Rev. Left. 33, 1406 (1974); *G. S. Abrams et al.:* Phys. Rev. Left. 33, 1453 (1974),

[6] *S. W. Herb et al.:* Phys. Rev. Lett. 9, 252 (1977)

[7] *R. Brandelik et al.:* Phys. Lett. 86B, 243 (1979); *D. P. Barber et al.:* Phys. Rev. Lett. 43, 830 (1979); *Ch. Berger et al.:* Phys. Lett. 86B, 418 (1979)

[8] *The Nobel Foundation:* The Nobel Prize in Physics 2008, [online]:
http://www.nobelprize.org/nobel_prizes/physics/laureates/2008
(cit. 2016/05/04)

[9] *The Nobel Foundation:* The Nobel Prize in Physics 2015, [online]:
http://www.nobelprize.org/nobel_prizes/physics/laureates/2015
(cit. 2016/05/04)

[10] *G. Anzivino et al. [NA48 Collaboration]:* Measurement of Direct CP Violation by NA48 arXiv:hep-ph/0111393

[11] *NA62 Collaboration:* Technical Design Document NA62-10-07, December 2010

[12] *A.J. Bevan et al.:* The Physics of the B Factories, arXiv:1406.6311 [hep-ex]

[13] *J Brodzicka at al. [Belle Collaboration]:* Prog. Theor. Exp. Phys. (2012) 04D001

[14] *Z. Dolezal, S. Uno et al.:* Technical Design Report, arxiv: 1011.0352v1,

[15] *Ch. Pulvermacher:* dE/dx particle identification and pixel detector data reduction for the Belle II experiment, Diploma thesis, Karlsruhe, 2012

[16] *M. Schnell:* The Belle II Pixel Detector for the SuperKEKB Flavour Factory, PoS(Vertex2014)016

[17] *J. Kemmer and G. Lutz:* Nucl. Instrum. Meth. Phys.Res. A 253, 356 (1987)

[18] *Max-Planck-Institut fur extraterrestrische Physik and Max-Plank-Institut fur Physik:* Research Activities [online]

[19] *P. Majewski:* Exp Astron (2014) 37:525–538

[20] *L. Bombelli, C. Fiorini, S. Facchinetti, M. Porro, G. De Vita:* A fast current readout strategy for the XFEL DePFET detector [online] http://dx.doi.org/10.1016/j.nima.2010.03.123 (cit. 2016/05/04)

[21] *M. Friedl, T. Bergauer, A. Frankenberger, I. Gfall, C. Irmler, M. Valentan:* The Silicon Vertex Detector of the Belle II Experiment [online] http://dx.doi.org/10.1016/j.phpro.2012.02.428 (cit. 2016/05/04)

[22] *Belle II Collaboration:* The vertex detector numbering scheme (Belle II internal document)

[23] *O. Frost:* A local tracking algorithm for the Central Drift Chamber of Belle II, Diploma thesis, Karlsruhe, 2013

[24] *L. Šantelj et al.* Aerogel RICH counter for the Belle II forward PID [online] http://dx.doi.org/10.1016/j.nima.2014.06.061 (cit 2016/05/04)

[25] *D. Y. Kim* Software and Physics Simulation at Belle II arXiv:1510.09008 [physics.ins-det]

[26] P. Urquijo, T. Ferber Overview of the Belle II Physics Generators (Belle II internal document)

[27] *Ch. Hagmann et al.:* Monte Carlo Simulation of Proton-included Cosmic-ray Cascades in the Atmosphere, [online] http://nuclear.llnl.gov/simulation/cry_physics.pdf, (cit. 2016/05/04)

[28] *M. Hohlmann et al.:* GEANT4 Simulation of a Cosmic Ray Muon Tomography System with Micro-Pattern Gas Detectors for Detection of High-Z Materials, arXiv:0811.0187 [physics.ins-det]

[29] *E. Niner:* Observation of electron neutrino appearance in the NuMi beam with the NOVA experiment, doctoral thesis, Indiana University, 2015

[30] *E. Aguayo et al.:* Cosmic Ray Interaction in Shielding Materials, PNNL-20693, 2011.

[31] M. Stoy Calibration and Alignment of the CMS Silicon Tracking Detector, Dissertation, University of Hamburg, 2007

[32] *V. Blobel, C. Kleinwort:* A new method for the high-precision alignment of track detectors, arXiv:hep-ex/0208021

[33] *V. Karimäki et al.* Sensor Alignment by Tracks, arXiv:physics/0306034 [physics.data-an]

[34] *C. Kleinwort:* General Broken Lines as advanced track fitting method arXiv:1201.4320 [physics.ins-det]

[35] *V. Blobel:* Nucl. Instrum. Meth. A566 (2006) 14-17

[36] *C. Kleinwort, H1 Collaboration:* Alignment Experiences, [online] http://webh06.cern.ch/lhc-detector-alignment-workshop/Proceedings/h1rep.pdf (cit. 2016/05/04)

[37] *CMS Collaboration,* Alignment of the CMS tracker with LHC and cosmic ray data, arXiv:1403.2286 [physics.ins-det], 2014

[38] *J. Kandra:* Alignment studies for the Belle II tracking system, [online] http://www.desy.de/f/students/2015/reports/JakubKandra.pdf (cit 2016/05/05)

[39] BaBar collaboration: Vertexing Control Samples (Collaboration internal document)

[40] *S. Wehle:* Private communication

[41] *O. Frost:* Private communication

List of Figures